Title: **Plain and notch fatigue strength of thick-walled ductile cast iron EN-GJS-600-3: A double-notch critical distance approach to defect sensitivity**

Authors: **M. Benedetti, C. Santus, V. Fontanari, D. Lusuardi, F. Zanini, S. Carmignato**

DOI Link: https://doi.org/10.1016/j.ijfatigue.2021.106414

Plain and notch fatigue strength of thick-walled ductile cast iron EN-GJS-600-3: a double-notch critical distance approach to defect sensitivity

Matteo Benedetti[1*], Ciro Santus[2], Vigilio Fontanari[1], Danilo Lusuardi[3], Filippo Zanini[4], Simone Carmignato[4]

[1]*Department of Industrial Engineering, University of Trento, via Sommarive 9, 38123 Trento, Italy*

[2]*Department of Civil and Industrial Engineering, University of Pisa, Pisa, Italy*

[3]*Fonderie Ariotti, Adro (BS), Italy*

[4]*Department of Management and Engineering, University of Padua, Vicenza, Italy*

*Corresponding author
Matteo Benedetti
matteo.benedetti@unitn.it

Abstract

In some fatigue critical scenarios, like those arising in cast or additively manufactured components, the fatigue damage mechanisms prevailing in plain and notched components might be different. This could hinder the applicability of the theory of critical distances (TCD), which postulates that the critical distance L can be inferred from a plain and a notched or cracked specimen configuration. To overcome this shortcoming, we explore in this work the possibility of inferring L from two notched geometries with different notch severity. The proposed method is applied to the notch fatigue prognosis of the ductile cast iron EN-GJS-600-3.

Keywords

Notch fatigue, defects, theory of critical distances, ductile cast iron

Nomenclature

$\sqrt{area}$	geometrical parameter of the defect
CT	computed tomography
D	notched specimen bar diameter
HV	Vickers hardness
K_r	ratio of the fatigue stress concentration factors
K_f	fatigue stress concentration factor
K_t	theoretical stress concentration factor
$K_{N,UU}$	notch stress intensity factor
L	critical length according to LM estimated from plain and notched specimen geometries

L^*	critical length according to LM estimated from two notched specimen geometries
$L^{*'}$	critical length according to PM estimated from two notched specimen geometries
LM	line method
L_{th}	critical length estimated from plain fatigue strength and crack growth threshold
L'	critical length according to PM estimated from plain and notched specimen geometries
l	dimensionless critical length according to LM
l_0	dimensionless singular term critical length according to LM
N_f	number of cycles to failure
PM	point method
R	load ratio
S	standard deviation
TCD	theory of critical distances
α	notch opening angle
ΔK_{th}	long crack growth threshold
$\Delta\sigma_{fl}$	plain fatigue strength range
$\Delta\sigma_{N,fl}$	notch fatigue strength range
$\Delta\sigma_{fl}^*$	intrinsic plain fatigue strength range
λ	ratio between notched specimens diameter
ρ	dimensionless notch root radius
$\sigma_{N,a}$	nominal stress amplitude on the net cross-section
σ_U	ultimate tensile strength
σ_Y	yield strength
σ_w	high cycle fatigue strength predicted by Murakami's model

Subscripts

1	sharp notch
2	blunt notch

1. Introduction

Defects, like surface roughness, inclusions, pores, foreign object damages, play a crucial role in fatigue crack initiation and propagation, impacting on the structural integrity of components exposed to time-varying loads. To this regard, fundamental investigations [1] were carried out since the 70s of the last century on conventionally manufactured materials, such as tool steels [2], cast Al-Si eutectic alloys [3], ductile cast iron (DCI) [4], [5], welded joints [6], as it was recognized that defects are the preferential fracture origin in such intrinsically flawed materials. Nowadays, the interest in encapsulating the defects effect into the fatigue design has further increased with the advent of additive manufacturing (AM) technologies, which, on one side, permit larger design freedom, on the other one, introduce into the component defects in the form of surface flaws and

irregularities, as well as pores and lack of fusion or gas entrapment [7]. Most of the fatigue assessments carried out so far rely on the pioneering work of Murakami [8], [9], whose well-known formula expresses the fatigue limit as function of the Vickers hardness and the defect $\sqrt{area}$ parameter. In materials with very inhomogeneous microstructure, like cast irons, the Vickers hardness turned out to be affected by large point-to-point variability and therefore poorly representative of the macroscopic fatigue properties of the material. For this purpose, Deguchi [10] and, more recently, Borsato et al. [11] proposed modifications of the Murakami formula, wherein the hardness is replaced by the tensile and/or the yield strength.

This scenario is further complicated by the fact that usually machine parts are not only weakened by defects but also by geometrical details (holes, grooves, key seats, etc.), in general denoted as "notches". They alter the lines of force flow resulting in local stress concentration that may promote the onset of fatigue damage. Dealing with the simultaneous effect of defects at the microscopic and of notches at the macroscopic level is not an easy task. For the sake of simplicity, the flawed material can be considered a homogenous medium with reduced fatigue properties. Its fatigue strength can be assessed by applying notch fatigue methods codified in machine design manuals and based on correction coefficients accounting for the geometrical stress concentration factor and the material's notch sensitivity [12]. The low value of the plain fatigue strength, as a consequence of the intrinsic material defectiveness, generally results in low notch sensitivity. If the notch fatigue is reinterpreted by the light of more sophisticated methods, such as the Theory of Critical Distances (TCD) [13] or based on the Strain Energy Density [14], [15], the low material's notch sensitivity can be explained by invoking the large value of the critical distance or the control radius of the material. However, these material characteristics turn out to be defect-dependent, therefore, a specific testing campaign is necessary to calibrate their value according to the defectiveness present in the vicinity of the notch [16], [17].

In the framework of TCD, which is the focus of the present work, three possible strategies to deduce the critical length L are schematically illustrated in Fig. 1. In the classical TCD formulation, L is determined by combining the long crack threshold ΔK_{th} and the plain fatigue limit range $\Delta\sigma_{fl}$:

$$L_{th} = \frac{1}{\pi}\left(\frac{\Delta K_{th}}{\Delta\sigma_{fl}}\right)^2 \tag{1}$$

Where the subscript "th" indicates that L is deduced from the crack threshold. However, this route (denoted in Fig. 1 as "Plain&Threshold") has some drawbacks, mainly related to the difficulty in accurately determining ΔK_{th} [18]. For instance, in the case of DCI, viz. the material investigated in this work, ΔK_{th} typically assumes very high values in comparison with other structural metallic materials, as a result of extrinsic fatigue crack growth resistance mechanisms [19]. Specifically, the crack path is made very tortuous due to the tendency of the crack to propagate adjacent to and not through the graphite nodules [20], [21]. However, the resulting crack shielding mechanism is fully deployed only when the crack is sufficiently long [22], [23]. For this reason, specific testing campaigns are necessary to identify such crack length threshold, making the experimental determination of ΔK_{th} even more challenging. In addition, given the crucial role played by the size and spatial distribution of graphite nodule, very different ΔK_{th} values can be found, especially in castings obtained at very long solidification times and affected by degeneration of the nodular graphite [24]. Therefore, it is not

surprising that a large spectrum of ΔK_{th} values was reported in the literature for DCI, ranging between 5 and 15 MPa·m$^{0.5}$ at R≈0 [19], [25], [26]. As a result, values of L_{th} ranging between 0.5 mm and 0.9 mm were reported for this material [27], [28]. Interestingly, these L_{th} values are approximately one order of magnitude higher than that of high strength aluminum alloys and steels [18]. This is not unexpected since DCI features a small plain specimen fatigue strength (because of its intrinsic defectiveness) along with high ΔK_{th} values.

To overcome these limitations, an alternative way, denoted in Fig. 1 as "Plain&Sharp", was devised by Santus et al. [29]. This is based on the knowledge of the fatigue strength of a plain and notched specimen geometry. This latter was optimized to maximize the intensity of the singular notch stress term and hence to minimize the sensitivity of the inverse search of critical distance to the experimental uncertainty. Analytical formulas were derived in [29] to determine the critical lengths L and L', according to the line (LM) and point method (PM), respectively, without the necessity of finite element analyses of the notch stress field. A probabilistic approach was then conceived in [30] to encapsulate the statistical variability of the input fatigue characteristics into the definition of L as a random variable. The method shown in Fig. 1b was successfully applied to structural metals like quenched+tempered steel and Al alloys [18], leading to a L estimation in good agreement with L_{th}. Conversely, when this approach was applied in [16] to additively manufactured Ti-6Al-4V, a large discrepancy between L and L_{th} was found. This was imputed to crack growth mechanisms different from those arising in notched samples and, more importantly, to the fact that the population of critical defects triggering the fatigue damage in plain and notched samples was found to be different in size and to depend on the route followed for the notch manufacturing. For this reason, the plain fatigue strength used in L inverse search was replaced by a fictitious value obtained through the Murakami model devised in [31] and incorporating the actual hardness and critical defect size found at the notch tip. The necessity of readapting the plain fatigue strength to the length scale of the fatigue damage occurring in notched components was also recently pointed out by He et al. [32]. Clearly, such approach requires a level of sophistication related to the necessity of statistically characterizing the distribution of defects in the neighborhood of the notch tip, which is hardly feasible at an industrial level. This scenario might be even more complicated in the notch fatigue prognosis of DCI, because this material is affected by a large spectrum of defect types, comprising graphite nodules, microshrinkage porosities and matrix structures composed of different phases [4], [33], [34]. It is therefore reasonable to expect that their role in originating the fatigue damage will be dissimilar in plain and notched samples, given the different size of the critically stressed volume, within which diverse defect types of different size might be present.

To correctly capture the length scale of the fatigue damage occurring in notched components made of intrinsically defected materials, the present work proposes a method, termed "Blunt&Sharp" in Fig. 1, which is based on the use of two optimized notched specimen geometries producing a different stress concentration factor. The fatigue characteristics determined in this way are therefore representative of the fatigue damage mechanism ruling the neighborhood of the notch tip. In this way, it is possible to deduce, along with the critical length L^*, an intrinsic plain fatigue strength $\Delta\sigma_{fl}^*$, which ideally represents the fatigue strength measured using miniaturized plain samples extracted from the notch tip. This paper is organized as follows: Section 2 illustrates

the procedure for inverse search of the critical distance L^* from two notched geometries according to the LM; this section further develops analytical formulas devised in [29] for the "Plain&Sharp" approach. Section 3 describes the DCI representative of heavy-section castings investigated in this work and the procedures for its experimental characterization. Section 4 illustrates the results of the fatigue tests and compares the outcomes of the three inversion strategies sketched in Fig. 1. Particular care is devoted to the identification of the fatigue damage mechanism acting in plain and notched samples through fractographic inspections of fatigue coupons and metrological X-ray computer tomography (CT) analyses of defects detected in the gage section of a plain sample. The proposed approach is validated through the prediction of the fatigue strength of independent notched geometries not used for the calibration of the TCD method. Concluding remarks are given in Section 5. The appendix reports the application of the "Blunt&Sharp" to the PM and illustrates an applicative example of its use according to LM and PM.

2. Critical distance inverse search from two notched specimen geometries

The proposed procedure is based on two notched geometries characterized by different non-dimensional notch root radii ρ_1, ρ_2, same notch angle α, either 90° or 60°, and same specimen outer diameter D. The meaning of these geometrical parameters is illustrated in Fig. 1. The fatigue strengths of the two notched variants are denoted as $\Delta\sigma_{\mathrm{N1,fl}}, \Delta\sigma_{\mathrm{N2,fl}}$. The plain intrinsic fatigue limit $\Delta\sigma_{\mathrm{fl}}^*$ is assumed to be unknown. The ratio of the fatigue stress concentration factors of the two specimens is:

$$K_{\mathrm{r}} = \frac{K_{\mathrm{f1}}}{K_{\mathrm{f2}}} = \frac{\Delta\sigma_{\mathrm{fl}}^*}{\Delta\sigma_{\mathrm{N1,fl}}} \frac{\Delta\sigma_{\mathrm{N2,fl}}}{\Delta\sigma_{\mathrm{fl}}^*} = \frac{\Delta\sigma_{\mathrm{N2,fl}}}{\Delta\sigma_{\mathrm{N1,fl}}} \tag{2}$$

Assuming that specimen "1" is sharper than "2", the ratio $K_{\mathrm{r}} > 1$ since $K_{\mathrm{f1}} > K_{\mathrm{f2}}$. This ratio K_{r} is the only experimental input required for the procedure. After the determination of the critical distance length, both K_{f1} and K_{f2} are obtained, and then the plain intrinsic fatigue limit $\Delta\sigma_{\mathrm{fl}}^*$ can be easily derived, from either $\Delta\sigma_{\mathrm{N1,fl}}$ or $\Delta\sigma_{\mathrm{N2,fl}}$.

More precisely, the critical distance L searched is the value corresponding to K_{f1} and K_{f2} for the two notch geometries. In principle, if the critical distance is very small, it reduces to the stress concentration factor ratio: $K_{\mathrm{t1}} / K_{\mathrm{t2}}$. On the contrary, for very large critical distances, both the two $K_{\mathrm{f1}}, K_{\mathrm{f2}}$ values tend to unity. Therefore, K_{r} is comprised in this range: $1 < K_{\mathrm{r}} < K_{\mathrm{t1}} / K_{\mathrm{t2}}$.

The search for the critical distance, starting from the ratio K_{r}, can be performed according to either LM or PM. The former has a linear formulation that reduces to a closed-form formula. On the contrary, the PM requires an iterative search described in the Appendix. Two dimensionless values are defined as: $l_1 = L^* / (D_1 / 2)$ and $l_2 = L^* / (D_2 / 2)$. After introducing a scale factor λ between the sizes of the two specimens, it follows:

$$\lambda = D_1 / D_2$$
$$l_2 = \lambda l_1 \tag{3}$$

Each dimensionless critical distance can be linearly related to singularity-based (dimensionless) lengths, which are referred to as $l_{0,1}$ and $l_{0,2}$:

$$l_1 = l_{\min,1} + (l_{0,1} - \gamma_{\min,1}) / \beta_1$$
$$l_2 = l_{\min,2} + (l_{0,2} - \gamma_{\min,2}) / \beta_2 \tag{4}$$

where $l_{\min}, \gamma_{\min}, \beta$ are specific to notch 1 and 2, and β is the slope of the linear expression $\beta = (\gamma_{\max} - \gamma_{\min}) / (l_{\max} - l_{\min})$ defined in [29]. All these coefficients are known parameters available in [29]. The two relations in Eq. (4) can be easily inverted and both sides divided:

$$\frac{l_{0,2}}{l_{0,1}} = \frac{\beta_2 (l_2 - l_{\min,2}) + \gamma_{\min,2}}{\beta_1 (l_1 - l_{\min,1}) + \gamma_{\min,1}} \tag{5}$$

Being the singularity-based length l_0 related to K_f for both specimens:

$$l_{0,1} = \frac{1}{2}\left(\frac{K_{N,UU}}{(1-s) K_{f1}} \right)^{1/s}$$
$$l_{0,2} = \frac{1}{2}\left(\frac{K_{N,UU}}{(1-s) K_{f2}} \right)^{1/s} \tag{6}$$

where $K_{N,UU}$ and s are the notch-stress intensity factor and the William's power law singularity exponent reported in [29] as a function of the notch opening angle α. The ratio between these two lengths reduces to:

$$\frac{l_{0,2}}{l_{0,1}} = K_r^{1/s} \tag{7}$$

After combing Eq. (5) and Eq. (7), the following equation is obtained:

$$\frac{\beta_1}{\beta_2} K_r^{1/s} = \frac{l_2 - b_2}{l_1 - b_1} \tag{8}$$

where: $b_1 = l_{\min,1} - \gamma_{\min,1} / \beta_1$ and $b_2 = l_{\min,2} - \gamma_{\min,2} / \beta_2$

and by substituting the simple relation between the two unknown lengths, Eq. (3) becomes a linear equation in the only unknown l_1. This turns out to be given by:

$$l_1 = \frac{b_1 \frac{\beta_1}{\beta_2} K_r^{1/s} - b_2}{\frac{\beta_1}{\beta_2} K_r^{1/s} - \lambda} \tag{9}$$

which can be then converted into the researched length:

$$L^* = l_1 \frac{D_1}{2} \tag{10}$$

After having solved and obtained the LM critical distance, the two K_f can be easily obtained. The singularity-based length is obtained from Eq. (4):

$$l_{0,1} = \beta_1 (l_1 - l_{\min,1}) + \gamma_{\min,1} \tag{11}$$

and then reversing again Eq. (6), K_{f1} can be easily found and then K_{f2} too:

$$K_{f1} = \frac{1}{1-s} \frac{K_{N,UU}}{(2 l_{0,1})^s}$$
$$K_{f2} = K_{f1} / K_r \tag{12}$$

Being the notched specimen fatigue limits known, the plain intrinsic fatigue limit is finally deduced such as from the notch 1:

$$\Delta\sigma_{fl}^{*} = \Delta\sigma_{N1,fl} K_{f1} \tag{13}$$

The LM critical distance inverse search according to LM will be applied in the following sections to the experimental data collected for the DCI under investigation.

3. Material and experimental procedures

The experimentation was performed on an EN-GJS-600-3 pearlitic ductile cast iron (DCI) of chemical composition listed in Table 1. The specimens were extracted from an as-cast cylinder (300 mm diameter, 520 mm height) of high thermal modulus (~6 cm) exposed to natural air convection, thus representative of thick-walled castings subjected to long solidification times [35], [36]. All the samples were taken from the bottom half of the cast cylinder in order to maintain a certain uniformity in microstructure and defectiveness.

The microstructure was characterized by conventional metallographic analyses. Samples were mounted and ground from 220 to 4000 mesh SiC abrasive papers. The final polishing was done using a 3-micron diamond paste followed by a 0.04-micron alumina suspension. Nital etching was used to reveal the microstructure. To characterize the graphite morphology of each material variant, quantitative image analysis was conducted with software ImageJ® on five cross-sections randomly extracted from the samples. Specifically, non-etched micrographs were binarized and elaborated with a particle analysis tool to measure area *A*, perimeter *U*, nearest neighbor distance λ_{nn}, and maximum Feret's diameter d_F of each graphite particle. The deviation from the spherical shape is estimated by the shape factor expressed as:

$$f_0 = \frac{4\pi A}{U^2} \tag{14}$$

and by roundness factor defined as:

$$\rho_G = \frac{4A}{\pi d_F^2} \tag{15}$$

The mean particle diameter of the graphite nodules is estimated as:

$$d_G = \sqrt{\frac{4A}{\pi}} \tag{16}$$

Finally, the graphite fraction was evaluated as the ratio between the total area of the graphite particles and the area of the metallographic micrograph. The fraction of spheroidal graphite was determined according to the approach set in [19], wherein the nearest neighbor distance λ_{nn} is used as discriminating factor between spheroidal and non-spheroidal graphite particle. For the present solidification condition, graphite nodules were categorized as spheroidal when $\lambda_{nn} \geq 45$ μm and and $f_0 \geq 0.35$.

Five monotonic tensile tests were carried out according to the standard UNI EN ISO 6892-1 on dog-bone coupons (14 mm gauge diameter, 84 mm parallel length), using a servo-hydraulic universal testing machine, equipped with hydraulic grips, and a load cell of 200 kN. The yield strength was determined as the 0.2% offset yield stress.

The fatigue characterization was conducted using the axisymmetric specimen geometries illustrated in Fig. 2a-e. Specifically, the plain (smooth) specimen geometry shown in Fig. 2a was used to determine the materials baseline fatigue S-N curve. V-notched specimen geometries reported in Fig. 2b-e are characterized by a notch depth, which was optimized in [29] to maximize the intensity of the asymptotic stress field term and therefore minimize the sensitivity of the inverse search of the critical distance to the experimental uncertainties. Specimens (b) and (c) have a notch opening angle of 60° and differ only in the notch tip radius, whose nominal value was set to 0.2 and 1 mm, respectively. In the following, they will be denoted as sharp and blunt notches. Two additional notched geometries, denoted (d) and (e) in Fig. 2, were selected to obtain independent fatigue data to be used to validate the predictions made applying the critical distance approaches illustrated in Fig. 1. Given the crucial role played by the notch root radius on the notch stress field, its actual value was verified by means of stereomicroscopic measurements and reported in Table 2 along with the corresponding theoretical stress concentration factor K_t. The measured notch root radii reported in Table 2 were used in the following TCD calculations.

Alternating (zero mean stress, load ratio R= −1) axial fatigue tests were carried out according to the ASTM E466 standard in a laboratory environment using a Rumul Testronic 50kN resonant testing machine, operating at a nominal frequency of 150 Hz under load control. Fatigue tests were therefore carried out at different stress amplitudes to explore the fatigue lives up to 5×10^6 cycles. The S-N curve for each experimental condition was obtained from at least 12 samples, and runout tests were terminated at 5×10^6 cycles when no fracture took place. The S-N curves were found to be well represented by the following model:

$$\sigma_a = k_1 + \frac{k_2}{N_f^{k_3}} \tag{16}$$

In fitting Eq. (16), only the run-out tests obtained at the highest explored stress level were included along with the tests ended after a failure. The scatter of the fatigue data was assessed by computing the estimated regression variance assumed to be uniform for the whole fatigue life range and expressed by:

$$S^2 = \frac{\sum_{i=1}^{n}\left(\sigma_{a,i} - \hat{\sigma}_{a,i}\right)^2}{n-p} \tag{17}$$

where $\sigma_{a,i}$ is the i-th fatigue amplitude data point, $\hat{\sigma}_{a,i}$ is its estimator, n is the number of data elements, and p is the number of parameters in the regression ($p = 3$ in the present case).

To check the effectiveness of this approach to robustly predict the high cycle fatigue (HCF) strength, sample batches (a), (d) and (e) were tested according to a staircase approach as well. In this way, the fatigue strength corresponding to a fatigue life of 5×10^6 cycles was evaluated employing 20 samples and 10 MPa stress increments.

The fracture surface of all the fatigue samples per each specimen geometry was analyzed using a JEOL JSM-IT300LV scanning electron microscope (SEM) to investigate the crack initiation site, taking particular care in identifying the microstructural feature triggering the fatigue damage. In addition, four fractured plain specimens (a) were scanned and analysed through metrological X-ray CT [37], using a Nikon Metrology MCT225 system. The system is characterized by micro-focus X-ray source with minimum focal spot size of 3 µm, 16-bit X-ray detector with a 2000×2000 grid of pixels and controlled cabinet temperature (20 ± 0.5 °C). Each CT scan consisted in the acquisition of 1500 bi-dimensional projections at different angular positions of the specimen performed with voltage 220 kV, current 36 µA and exposure time 2 s. Importantly, the small gage diameter of the specimens allowed scanning their entire volume with high structural resolution [38], which is needed to detect and measure micro-features such as internal voids and graphite spheroids. In particular, the achieved voxel size (i.e. volumetric pixel) was equal to 5.8 µm and the low X-ray beam power involved (below 8 watts) resulted in a minimal focal spot size. The beam hardening effect - which often generate image artifacts in CT reconstructions [39] - was reduced using a 0.1 mm-thick physical filter made of copper and by subsequent software correction using the following polynomial: $y = 1.94(0.5x^2 + 0.5x)$,, where x represents the initial grey value of a pixel and y represents the corrected grey value. The acquired projections were then reconstructed using a filtered backprojection algorithm [40] and the visualization and analysis software VGStudio MAX 3.2 (Volume Graphics, GmbH) was used to detect and measure internal voids as well as graphite nodules in terms of dimensions, shape and position. The shape was evaluated by computing pores and nodules sphericity ϕ, defined as:

$$\phi = \frac{\pi^{1/3}\left(6V\right)^{2/3}}{A} \tag{18}$$

where A and V are pore or nodule area and volume, respectively. The volume V was used to determine the mean diameter d^* as well:

$$d^* = \sqrt[3]{\frac{6V}{\pi}} \tag{19}$$

The mechanical characterization of the material was complemented by a fatigue crack growth (FCG) rate test conducted according to the ASTM E647standard. To reproduce the same fully reversed stress cycle of the Wöhler fatigue tests, the M(T) specimen geometry shown in Fig. 2f was used. Specifically, the FCG test was conducted in the laboratory environment on a Rumul Mikrotron 20 kN resonant testing machine under sinusoidal load waveform applied at a frequency of approximately 150 Hz. A Fractomat® apparatus based on the indirect potential drop method is used to continuously measure the crack extension from both tips. More

details about the experimental procedure are given in [16]. In brief, the test was conducted in two phases, the first one according to a force-shedding procedure until reaching near-threshold FCG conditions; after three consecutive crack growth increments resulting in a crack growth rate below 2×10^{-10} m/cycle, the second phase at constant force amplitude was started. The experimental da/dN - ΔK data were least-square fitted using the following expression proposed by Klesnil and Lukáš [41]:

$$\frac{da}{dN} = C\left(\Delta K^{m} - \Delta K_{\text{th}}^{m}\right) \tag{20}$$

where C and m are fitting coefficients and ΔK_{th} is the crack growth threshold.

4. Results and discussion

4.1 Optical microstructural analyses and monotonic tensile tests

The optical micrographs shown in Fig. 3a–b at two magnification scales illustrate the typical microstructure of the investigated material. The matrix is predominantly pearlitic, while ferritic layers surround the graphite nodules. Graphite particles of different size and shape are unevenly interspersed in the metallic matrix. The results of graphite quantitative and morphological 2D analyses are summarized in Table 3. Importantly, the graphite is almost completely present in the form of spheroidal nodules, while degenerated (mainly chunky) graphite is nearly absent. Shape factor and roundness take large values (well above 0.5), thus indicating that the graphite nodules have an approximately spherical shape with a mean diameter of about 60 μm.

The characteristic strength parameters obtained by conventional tensile tests and hardness measurements are reported in Table 4 and compared with guidance values prescribed by [42] on the mechanical properties measured on samples cut from moderately thick-walled castings (60 mm < t ≤ 200 mm) of EN-GJS-600-3. It can be noted that the investigated material is compliant with the guidance values in all the properties apart from the ultimate tensile strength. Apparently, the solidification conditions of the investigated material (corresponding to heavy-section castings) led to a non-optimal microstructure, affected, as shown below, by shrinkage porosity, which impacts detrimentally on the material ductility.

4.2 Fatigue and crack growth rate tests

The results of the axial fatigue tests carried out on all the specimen variants are compared in Fig. 4a. Fitting curves corresponding to 50% (solid line), 10% and 90% (dashed lines enclosing a colored scatter band) failure probability, expressed by Eq. (16), are also plotted in Fig. 4. The best-fit parameters and the standard deviation S are listed in Table 5, which compares, where available, the estimation of the fatigue strength at 5×10^{6} cycles made according to Eq. (16) and the staircase approach. Importantly, the two fatigue assessment methods led to very similar values, especially in terms of mean value. In view of this result, the HCF strength estimations made for specimens (b) and (c) using only Eq. (16) are deemed to be reliable as well.

Looking at Fig. 4, it can be noted that the plain fatigue data are affected by a considerable scatter (coefficient of variation of about 12%), significantly larger than that of the notched counterparts (comprised between 4 and 8%). The fatigue curves of the notched variants approximately scale according to the notch stress concentration

factor K_t, apart the geometry (e), which displays a superior fatigue strength with respect to that expected from K_t. Apparently, the small specimen diameter results in a more localized and thus less detrimental notch stress field, as further discussed in the following.

The d*a*/d*N*-ΔK FCG curve is plotted in Fig. 4b. Table 6 reports the best-fit parameters of Eq. (20). Interestingly, the obtained crack growth threshold is only a few MPa·m$^{0.5}$ higher than the values reported in [19] for a similar DCI tested under positive load ratios R. Evidently, the compressive part of the load cycle as well contributes to the fatigue crack extension. In addition, the obtained value of 14.0 MPa·m$^{0.5}$ is in good agreement with the value 14.3 MPa·m$^{0.5}$ found by Zambrano et al. [26] for DCI at R=-1 employing a specimen of size comparable to that shown in Fig. 2f.

4.3 Inverse search of the critical distance and notch HCF strength predictions

The results of the inverse search of the LM critical distance are summarized in Table 7 for the three approaches discussed in the Introduction and sketched in Fig. 1. Importantly, the two approaches based on the plain fatigue limit (namely "Plain&Threshold" and " Plain&Sharp") predict a very large value of the critical distance, above 0.5 mm, well above the values typically reported in the literature [13], [16], [18] for structural metallic materials. Conversely, the approach "Blunt&Sharp" based on two notched specimen geometries leads to estimate a much shorter critical distance L^*, about 0.14 mm, and an intrinsic plain fatigue strength $\Delta\sigma_{fl}^*/2$ (about 270 MPa) significantly higher than that displayed by the plain samples (a). The predictions listed in Table 9 of the HCF strength of independent notched variants permit to assess the suitability of these three critical distance approaches to predict the notch fatigue resistance of DCI. A systematic comparison is possible only for variants (d) and (e), used in neither of these approaches. Interestingly, the "Blunt&Sharp" approach is the only one able to keep the absolute relative error well below 10%. In particular, the high value of the fatigue strength of the small diameter notch variant (e) (only 20% lower than the plain fatigue strength) is correctly predicted as well, despite the great K_t (4.48) affecting this geometry. Evidently, the large value of the critical distance exhibited by DCI is able to attenuate a lot the average notch stress field localized in few mm tenths ahead of the notch tip.

Conversely, the "Plain&Threshold" and "Plain&Sharp" predictions are affected by larger errors, even up to 16%. In addition, errors of comparable magnitude affect the predictions of the blunt notched variant (b). Evidently, these latter two approaches are influenced by fatigue damage mechanisms occurring in plain and M(T) specimens that are scarcely representative of those taking place in notched coupons. Interestingly, the fact that the "Blunt&Sharp" approach predicts the crack growth threshold with higher error with respect to the "Plain&Sharp" method supports the idea that the fatigue damage conditions occurring at the notch tip significantly deviate from those taking place in plain [5] and cracked [20] components. To shed light on these aspects, the next section will discuss the results of fractographic analyses and CT scans.

4.4 Fractographic and defectiveness analysis

SEM analyses were conducted to identify the dominant crack initiation mechanisms acting in the HCF regime. A meaningful example of the crack initiation site found in plain (a) specimens is reported in Fig. 5a. Importantly, in all the investigated smooth samples, the crack was found to initiate in the vicinity of a large solidification shrinkage pore (indicated by an arrow in Fig. 5a). The scenario depicted by the fracture surface of the notched variants (Fig. 5b-d) is completely different. Despite careful search, no shrinkage microporosity was found in the neighborhood of any fatigue crack initiation site at the tip of the notched samples. The fracture surface reported in Fig. 5b indicates that the crack nucleated from a large graphite nodule (red arrow in Fig. 5b) located in the vicinity of the notch tip. However, the smearing action exerted by the fully-reversed stress cycle on the fracture surface eliminated characteristic features (striations, beach marks, etc.) permitting to unambiguously identify the graphite nodule as the microstructural constituent originating the fatigue damage. To overcome this difficulty, some notched samples survived after 5×10^6 cycles were retested by applying tension-tension (R=0.1) stress cycles until final failure. An example of the obtained fracture surface is shown at two magnifications in Fig. 5c and d. The dashed line in Fig. 5c indicates the front of the non-propagating crack nucleated in the run-out test. Its morphology is much less deteriorated with respect to that shown in Fig. 5b so that the striations particularly visible in Fig. 5d clearly point out that the crack nucleated from the graphite nodule indicated by the red arrow.

CT scans performed on plain samples provide a convincing interpretative key of the above-described scenario. Figure 6a illustrates the CT scan data image of a fatigued plain specimen (a). Shrinkage microporosity is highlighted in a color scale expressing the pore volume. It can be noted that the fatigue fracture (grey shaded surface in the middle) originated from the largest pore present in the gage volume of the specimen. In addition, pores are of much larger size and much lesser amount with respect to graphite nodules (darker grey particles), as summarized in Table 9. Importantly, in the gage volume 14 pores vs. 68537 graphite nodules were detected, displaying a mean diameter about 5 times larger and much lower sphericity (and presumably higher stress concentration factor) with respect to the latter ones. Interestingly, mean diameter and sphericity of graphite nodules evaluated through CT scans are in very good agreement with mean diameter and roundness summarized in Table 3 as a result of 2D optical measurements.

From the above discussion, it is not surprising that when the scanned gage volume is subjected to the uniform stress field reigning in smooth samples, the fatigue damage starts from the most critical pore. Conversely, if such gage volume is machined to introduce a stress raising geometrical feature (notch), two competing fatigue crack nucleation mechanisms take place: one located at the most critical pore and the other at the tip of the geometrical stress concentrator. In general, this latter crack initiation mechanism prevails in notched components made of cast iron, as the ubiquitous presence of graphite nodules inside the gage volume makes it possible that some of them are exactly situated in the vicinity of the notch tip, hence further increasing the stress concentration exerted by the notch. This explains the above-described fractographic evidence in the notched variants, attesting crack initiation from a graphite nodule in the vicinity of the notch tip. It is therefore clear that the approach "Blunt&Sharp" permits to determine the critical distance from two fatigue characteristics representative of the fatigue damage occurring at the notch tip, while this phenomenon is not

adequately captured by the other two inverse search approaches. It is therefore sensible that the first approach leads to more accurate predictions of the HCF strength of independent notched variants.

From the fractographic analysis, it can be argued that the graphite nodules play a crucial role in dictating the notch fatigue strength of DCI. To this regard, Figure 6b plots the bin histogram of the $\sqrt{area}$ Murakami parameter [8] of the graphite nodules detected in the whole CT reconstructed gage volume. The distribution is bimodal with a long right tail. The maximum $\sqrt{area}$ value is about 250 μm. Clearly, such value is not representative of the scenario occurring at the tip of the notched specimen, wherein the size of the critically stressed volume is much smaller. For this reason, it seems to be more appropriate to analyze the distribution of graphite nodules in a material volume of size linked to the critical distance found in the previous section. This idea is sketched in Fig. 7a, viz. only the graphite nodule population comprised within a toroidal control volume (red line) centered on the notch tip of the notched sample (blue line) is supposed to control its fatigue damage. Since it was possible to analyze via CT scans only plain samples (black line) and since notched specimens were turned from the same base material, it is reasonable to center such control volume on the outer surface of the plain sample. Figure 7b plots the bin histogram of the Murakami parameter $\sqrt{area}$ of the graphite nodules detected in control volumes of size a equal to $2L^*$ (viz. the same size of the notch stress averaging domain) located at three different axial locations z_c (see Fig. 6a and 7a for the location of the reference frame). Notably, no pore was detected in such control volumes (thus confirming their marginal role in dictating the notch fatigue strength); moreover, the size distribution of graphite nodules deviates significantly from that plotted in Fig. 6b for the whole scanned gage volume. Clearly, the total amount of nodules is much lower, the right tail of the distribution is even more elongated, and the maximum nodule size (about 150 μm) is considerably smaller. To get a more robust estimation of the maximum size of the graphite nodule expected in the control volume, the population of graphite nodules therein comprised was elaborated according to the statistics of largest extreme value distribution (LEVD) using the Maximum Likelihood Method [8], [43]. The statistical distribution of defect sizes obtained taking $a = 2L^*$ is shown in Fig. 7c. It can be noted that the maximum expected nodule size $\sqrt{area}_{\max}$ corresponding to a cumulative probability F of 99% is similar in the three control volumes and approximately equal to 155 μm. This value is in good agreement with the size of the nodule shown in Fig. 5b (about 140 μm) which triggered the fatigue failure of a notched specimen. It is also interesting to observe that the nodule shown in Fig. 5d, which was found to initiate a non-propagating crack in a runout specimen, is considerably smaller (about 80 μm). All this evidence supports the hypothesis that the largest graphite nodule in the control volume ahead of the crack tip controls the notch fatigue strength. Figure 7c plots the distribution of $\sqrt{area}_{\max}$ as a function of the radius a of the toroidal control volume. As expected, $\sqrt{area}_{\max}$ increases with a and, interestingly, tends to saturate at a values exceeding $2L^*$.

In light of these observations, we tried to predict the fatigue strength of the material encompassed within the control volume using the following $\sqrt{area}$ models proposed in the literature and successfully applied to DCI [8], [10], [11]:

$$\sigma_{\mathrm{W}} = \frac{F_{loc} F_{M}}{\left(\sqrt{area}_{\max}\right)^{1/6}}$$

$$F_{\mathrm{M}} = \begin{cases} HV + 120 & \text{Murakami } [8] \\ 0.34 \cdot S_{\mathrm{U}} + 170 & \text{Deguchi et al. } [10] \\ 0.62 \cdot S_{\mathrm{U}} + 0.32 \cdot S_{\mathrm{Y}} & \text{Borsato et al. } [11] \end{cases} \tag{21}$$

$$F_{\mathrm{loc}} = \begin{cases} 1.43 & \text{Surface defect} \\ 1.41 & \text{Near surface defect} \\ 1.56 & \text{Internal defect} \end{cases}$$

Where σ_W is the predicted fully-reversed HCF strength (expressed in MPa), F_{loc} is the location factor, F_M is a material strength parameter, usually defined as a function of Vickers hardness HV or monotonic tensile properties S_U and S_Y. Table 10 summarizes the predictions of the HCF strength of the material comprised in the control volume according to the three proposed models. In this analysis, the defects were assumed to be internal (F_{loc} = 1.56) as the fractographic inspections (see for instance Fig. 5b) located most of the critical nodules at a distance below the surface larger than their maximum Feret's diameter. It can be noted that the values of σ_W reported in Table 10 are significantly higher than the plain HCF strength listed in Table 5, as a result of the different size of the defect (graphite nodule vs. pore) triggering the fatigue damage. Interestingly, the value of σ_W predicted by Borsato et al. method (specifically devised for cast iron) is identical to that of the intrinsic plain fatigue strength $\Delta\sigma_{\mathrm{fl}}^{*}/2$ estimated through the double notch inversion method, thus confirming the suitability of this approach to predict the notch fatigue strength of DCI.

4.5 Extension of the "Blunt&Sharp" method to the medium cycle fatigue regime

As already discussed in [44], one of the advantages of deriving the critical distance from notched instead of cracked specimen geometries is the possibility of extending the TCD method to the medium cycle fatigue regime. Given the higher accuracy ensured by the "Blunt&Sharp" method, for the sake of brevity, we will extend only this latter approach to this fatigue regime. For this purpose, L^* and $\Delta\sigma_{\mathrm{fl}}^{*}/2$ are deduced from the method illustrated in Section 1, wherein K_r is estimated from sharp- (b) and blunt- (c) notch fatigue data taken at different fatigue lives N_f. Fig. 8a illustrates the variation of L^* (black solid line) and $\Delta\sigma_{\mathrm{fl}}^{*}/2$ (red dashed line) as a function of N_f. Interestingly, the critical length L^* is fairly independent of N_f, in contrast with the decreasing trend we found in other structural metallic materials [16], [44]. As expected, the intrinsic plain fatigue strength $\Delta\sigma_{\mathrm{fl}}^{*}/2$ decreases with increasing number of cycles to failure. Figure 8b plots the SN curves calculated for the two independent notched geometries (d) and (e). The predicted SN curves are in good agreement with the trend of the experimental data, especially for the variant (d), where the experimental data (dotted values) are uniformly dispersed above and below the predicted curve. Conversely, the predictions of the variant (e) are affected by an average overestimation of about 15%, nevertheless reasonable given the large uncertainty in the fatigue properties of the investigated material.

5. Conclusions

This paper explored the fatigue strength of a ductile cast iron (DCI) EN-GJS-600-3 fabricated under conditions representative of heavy-section castings. A significant difference was found in the defectiveness triggering the fatigue damage. In plain samples, a few shrinkage pores were found in the gage section through CT analyses. The largest pore is responsible for the fatigue crack initiation. In notched samples, the likelihood that such critical pore is located in the process zone ahead of the notch tip is very low, therefore the fatigue damage is promoted by the largest graphite nodule therein located. This evidence must be taken into account when applying a critical distance approach to predict the fatigue strength of DCI. For this purpose, instead of deriving the critical length from a plain specimen geometry affected by a fatigue mechanism not representative of that occurring at the notch tip, a novel inverse search is proposed in this paper. This is based on the use of two optimized notched geometries differing in notch root radius and hence in the resulting stress concentration factor. Analytical formulas for such inversion have been proposed in Section 2 for the line method and used for the fatigue calculation of independent notched geometries. A better agreement with the experimental data has been found with respect to predictions made with critical distance estimations based on the plain fatigue strength. The extension of the double notch inversion search to the point method is presented in the appendix for future use of this methods to other fatigue scenarios similar to that presented in this work.

We expect a transition in the defect originating the fatigue damage in notched geometries with declining notch severity from graphite nodule to microshrinkage porosity. In addition, we cannot exclude a priori the very infrequent case of a critical pore located at the tip of a sharp notch and triggering the fatigue damage instead of more frequent but less critical graphite nodules. All these circumstances necessitate a sound statistical approach that will be matter of future investigations.

Appendix

A.1 Point Method search

A similar inversion procedure was developed for the Point Method. An inversion procedure was developed for the Point Method in similarity with that proposed above for the Line Method. The initial unknown of the problem is again the fatigue stress concentration factor ratio K_r, however, the inversion procedure for the PM does not lead to a closed-form equation. The proposed approach is to define an appropriate search range and compare the deduced critical distances. In order to define an appropriate search range, the maximum fatigue stress concentration factor was determined, which obviously is the theoretical stress concentration factor K_t. Fig. A.1 shows the trend of the K_t for two investigated angles, as functions of the radius ratio ρ, and a fitting model for each trend.

An effective form for the stress concentration factor fit function was obtained after the observation that in log-log coordinates the relation between the radius ratio ρ and K_t is almost a linear, with small tendency of a parabola, thus three coefficients only were considered. The numerical model proposed to accurately fit the FE data is:

$$E_{\mathrm{K}} = t_1(\log_{10}(\rho))^2 + t_2 \log_{10}(\rho) + t_3$$
$$K_{\mathrm{t}} = 10^{E_{\mathrm{K}}} \tag{A.1}$$

where the use of the logarithm with base 10 was suggested by the radius ratio, which ranges from 0.01 to 1.0. However, the same fitting model would have been obtained with any other basis, and the same values of the three coefficients t_1, t_2, t_3 would result. These fitting coefficients are reported in Table A.1.

To propose an initial guess value for the length search, one of the two notches can be assumed as that with maximum notch sensitivity, and realistically this can be applied to the blunter notch, which is assumed as notch 2. Thus, the initial assumption $K_{\mathrm{f2}} = K_{\mathrm{t2}}$ can be proposed to set a starting point. Then the singularity-based length is obtained, according to this value of K_{f}, which in principle is corresponding to a null critical distance:

$$l'_{0,\min 2} = 2\left(\frac{K_{\mathrm{N,UU}}}{K_{\mathrm{t2}}}\right)^{1/s} \tag{A.2}$$

while for the maximum of the searching range, a value as large as the previous $\gamma_{\max}$ for notch 2, can be considered, which is usually quite large with respect to the material usual lengths:

$$l'_{0,\max 2} = \gamma_{\max,2}$$

Now, an iterative search can be performed by sampling this min. to max. range in many divisions, such as 10^4. The singularity-based length for the other notch is easily found with the same relationship of Eq. (7), which is equally valid for the PM:

$$l'_{0,\min 2} \le l'_{0,2} \le l'_{0,\max 2}$$
$$l'_{0,1} = l'_{0,2} / K_{\mathrm{r}}^{1/s} \tag{A.3}$$

And for each pf the tentative couples $l'_{0,1}$ and $l'_{0,2}$, the corresponding PM critical distances are:

$$l'_1 = \sum_{i=1}^{5} \delta_{i,1}\, l'^{5-i}_{0,1}$$
$$l'_2 = \sum_{i=1}^{5} \delta_{i,2}\, l'^{5-i}_{0,2} \tag{A.4}$$

where $\delta_{i,1}$ and $\delta_{i,2}$ are the PM coefficients, from [29], for the notch geometries 1 and 2, respectively. The objective function of this search is the difference of the two lengths, in dimensionless form and scaled, which is to be minimized as absolute value:

$$l'_2 = \lambda\, l'_1 \leftrightarrow \mathrm{Min.}(|l'_2 - \lambda\, l'_1|) \tag{A.5}$$

In the range proposed above, the two lengths are independently obtained, with Eq. (A.4), and then the couple of l'_1, l'_2 minimizing the difference of Eq. (A.5) can be iteratively found. After this minimization search, one of the two lengths, can be used for the final determination of the PM critical distance:

$$L^{*\prime} = \frac{D_2}{2} l'_2 \tag{A.6}$$

A.2 An applicative example

An example is reported here to show the proposed procedures of critical distance determination both according to the LM and the PM with two notches of different sharpness. The considered example is referring to the experimental data presented above, with the following data:

$$\begin{aligned} &D_1 = 20\,\text{mm}, \quad R_1 = 0.3\,\text{mm} \ \ (\text{Sharp}) \\ &D_2 = 20\,\text{mm}, \quad R_2 = 1.0\,\text{mm} \ \ (\text{Blunt}) \\ &K_\text{r} = \frac{\Delta\sigma_{\text{N2,fl}}}{\Delta\sigma_{\text{N1,fl}}} = \frac{236}{190} = 1.242 \end{aligned} \tag{A.7}$$

In this situation, the scale factor is not required ($\lambda = 1$) since both specimens were manufactured with the same external diameter D. According to the LM the following results are obtained:

$$\begin{aligned} &K_{\text{f1}} = 2.833 \\ &K_{\text{f2}} = 2.281 \\ &L^* = 0.1358\,\text{mm} \end{aligned} \tag{A.8}$$

Similar results are then found, in terms of K_f, according to the PM, while a larger critical distance is obtained:

$$\begin{aligned} &K_{\text{f1}} = 2.948 \\ &K_{\text{f2}} = 2.374 \\ &L^{*\prime} = 0.2005\,\text{mm} \end{aligned} \tag{A.9}$$

Figure A.2 shows the LM and PM relationships between the ratio K_r and the corresponding critical distances, and as discussed above, vary large (an unrealistic) length values are obtained for $K_\text{r} = 1$.

After the availability of the fatigue stress concentration factors, and the fatigue limits of the notched specimens, the plain intrinsic fatigue limit can be deduced. The same value is obtained from either specimen 1 or specimen 2, however, a small difference results between Line and Point Methods:

$$\begin{aligned} &\text{LM: } \Delta\sigma_{\text{fl}}^* = K_{\text{f1}}\,\Delta\sigma_{\text{N1,fl}} (= K_{\text{f2}}\,\Delta\sigma_{\text{N2,fl}}) = 538\,\text{MPa} \\ &\text{PM: } \Delta\sigma_{\text{fl}}^* = K_{\text{f1}}\,\Delta\sigma_{\text{N1,fl}} (= K_{\text{f2}}\,\Delta\sigma_{\text{N2,fl}}) = 560\,\text{MPa} \end{aligned} \tag{A.10}$$

References

[1] S. Usami and S. Shida, “Elastic–Plastic Analysis of the Fatigue Limit for a Material With Small Flaws,” *Fatigue Fract. Eng. Mater. Struct.*, vol. 1, no. 4, pp. 471–481, May 1979, doi: 10.1111/j.1460-2695.1979.tb01334.x.

[2] Y. Murakami and M. Endo, “Effects of defects, inclusions and inhomogeneities on fatigue strength,” *Int. J. Fatigue*, vol. 16, no. 3, pp. 163–182, Apr. 1994, doi: 10.1016/0142-1123(94)90001-9.

[3] I. Serrano-Munoz, J.-Y. Buffiere, C. Verdu, Y. Gaillard, P. Mu, and Y. Nadot, “Influence of surface and internal casting defects on the fatigue behaviour of A357-T6 cast aluminium alloy,” *Int. J. Fatigue*, vol. 82, pp. 361–370, Jan. 2016, doi: 10.1016/j.ijfatigue.2015.07.032.

[4] M. Endo and K. Yanase, “Effects of small defects, matrix structures and loading conditions on the fatigue strength of ductile cast irons,” *Theor. Appl. Fract. Mech.*, vol. 69, pp. 34–43, Feb. 2014, doi: 10.1016/j.tafmec.2013.12.005.

[5] P. Ferro, P. Lazzarin, and F. Berto, “Fatigue properties of ductile cast iron containing chunky graphite,” *Mater. Sci. Eng. A*, vol. 554, pp. 122–128, Sep. 2012, doi: 10.1016/j.msea.2012.06.024.

[6] S. C. Wu, Z. Song, G. Z. Kang, Y. N. Hu, and Y. N. Fu, “The Kitagawa-Takahashi fatigue diagram to hybrid welded AA7050 joints via synchrotron X-ray tomography,” *Int. J. Fatigue*, vol. 125, pp. 210–221, Aug. 2019, doi: 10.1016/j.ijfatigue.2019.04.002.

[7] N. Sanaei and A. Fatemi, “Defects in additive manufactured metals and their effect on fatigue performance: A state-of-the-art review,” *Prog. Mater. Sci.*, vol. 117, p. 100724, Apr. 2021, doi: 10.1016/j.pmatsci.2020.100724.

[8] Y. Murakami, *Metal fatigue: effects of small defects and nonmetallic inclusions.* Oxford: Elsevier, 2002.

[9] Y. Murakami, T. Takagi, K. Wada, and H. Matsunaga, “Essential structure of S-N curve: Prediction of fatigue life and fatigue limit of defective materials and nature of scatter,” *Int. J. Fatigue*, vol. 146, p. 106138, May 2021, doi: 10.1016/j.ijfatigue.2020.106138.

[10] T. Deguchi, T. Matsuo, H. Kim, T. Ikeda, and M. Endo, “Fatigue Strength Evaluation of Ferritic-Pearlitic Ductile Cast Iron with Notches and Holes of Various Sizes,” *Adv. Exp. Mech.*, vol. 2, pp. 87–91, 2017, doi: 10.11395/aem.2.0_87.

[11] T. Borsato, P. Ferro, and F. Berto, “Novel method for the fatigue strength assessment of heavy sections made by ductile cast iron in presence of solidification defects,” *Fatigue Fract. Eng. Mater. Struct.*, vol. 41, no. 8, pp. 1746–1757, Aug. 2018, doi: 10.1111/ffe.12815.

[12] R. Budynas and J. Nisbett, *Shigley’s mechanical engineering design*, 10th ed. McGraw-Hill Education, 2014.

[13] D. Taylor, *The Theory of Critical Distances. A New Perspective in Fracture Mechanics*, 1st ed. Elsevier Science, 2007.

[14] F. Berto, S. M. J. Razavi, and J. Torgersen, “Frontiers of fracture and fatigue: Some recent applications of the local strain energy density,” *Frat. ed Integrità Strutt.*, vol. 12, no. 43, pp. 1–32, Dec. 2017, doi: 10.3221/IGF-ESIS.43.01.

[15] P. Ferro, T. Borsato, F. Berto, and C. Carollo, “Fatigue strength assessment of heavy section ductile irons through the average strain density energy criterion,” *Mater. Des. Process. Commun.*, p. mdp2.197, Aug. 2020, doi: 10.1002/mdp2.197.

[16] M. Benedetti and C. Santus, “Notch fatigue and crack growth resistance of Ti-6Al-4V ELI additively manufactured via selective laser melting: A critical distance approach to defect sensitivity,” *Int. J. Fatigue*, vol. 121, no. December 2018, pp. 281–292, 2019, doi: 10.1016/j.ijfatigue.2018.12.020.

[17] M. Benedetti, M. Dallago, and C. Santus, “Statistical significance of notch fatigue prognoses based on the strain-energy–density method: Application to conventionally and additively manufactured

materials," *Theor. Appl. Fract. Mech.*, vol. 109, p. 102720, Oct. 2020, doi: 10.1016/j.tafmec.2020.102720.

[18] C. Santus, D. Taylor, and M. Benedetti, "Experimental determination and sensitivity analysis of the fatigue critical distance obtained with rounded V-notched specimens," *Int. J. Fatigue*, vol. 113, pp. 113–125, Aug. 2018, doi: 10.1016/j.ijfatigue.2018.03.037.

[19] M. Benedetti, V. Fontanari, and D. Lusuardi, "Effect of graphite morphology on the fatigue and fracture resistance of ferritic ductile cast iron," *Eng. Fract. Mech.*, vol. 206, pp. 427–441, Feb. 2019, doi: 10.1016/j.engfracmech.2018.12.019.

[20] V. Di Cocco, F. Iacoviello, A. Rossi, M. Cavallini, and S. Natali, "Graphite nodules and fatigue crack propagation micromechanisms in a ferritic ductile cast iron," *Fatigue Fract. Eng. Mater. Struct.*, vol. 36, no. 9, pp. 893–902, Sep. 2013, doi: 10.1111/ffe.12056.

[21] J. Hosdez *et al.*, "Fatigue crack growth in compacted and spheroidal graphite cast irons," *Int. J. Fatigue*, vol. 131, p. 105319, Feb. 2020, doi: 10.1016/j.ijfatigue.2019.105319.

[22] M. Benedetti, E. Torresani, V. Fontanari, and D. Lusuardi, "Fatigue and Fracture Resistance of Heavy-Section Ferritic Ductile Cast Iron," *Metals (Basel).*, vol. 7, no. 3, p. 88, Mar. 2017, doi: 10.3390/met7030088.

[23] M. Benedetti, J. Heidemann, J. O. Peters, and G. Lütjering, "Influence of sharp microstructural gradients on the fatigue crack growth resistance of α + β and near-α titanium alloys," *Fatigue Fract. Eng. Mater. Struct.*, vol. 28, no. 10, pp. 909–922, Oct. 2005, doi: 10.1111/j.1460-2695.2005.00932.x.

[24] L. Ceschini *et al.*, "Microstructure and mechanical properties of heavy section ductile iron castings: experimental and numerical evaluation of effects of cooling rates," *Int. J. Cast Met. Res.*, vol. 28, no. 6, pp. 365–374, Nov. 2015, doi: 10.1179/1743133615Y.0000000022.

[25] M. Dahlberg, "Fatigue crack propagation in nodular graphite cast iron," *Int. J. Cast Met. Res.*, vol. 17, no. 1, pp. 29–37, Jan. 2004, doi: 10.1179/136404604225012398.

[26] H. R. Zambrano, G. Härkegård, and K. F. Stärk, "Fracture toughness and growth of short and long fatigue cracks in ductile cast iron EN-GJS-400-18-LT," *Fatigue Fract. Eng. Mater. Struct.*, vol. 35, no. 4, pp. 374–388, Apr. 2012, doi: 10.1111/j.1460-2695.2011.01628.x.

[27] D. Taylor, M. Hughes, and D. Allen, "Notch fatigue behaviour in cast irons explained using a fracture mechanics approach," *Int. J. Fatigue*, vol. 18, no. 7, pp. 439–445, Oct. 1996, doi: 10.1016/0142-1123(96)00018-7.

[28] P. Livieri, E. Maggiolini, and R. Tovo, "On the notch sensitivity of cast iron under multi-axial fatigue loading," *Frat. ed Integrità Strutt.*, vol. 8, no. 30, pp. 558–568, Sep. 2014, doi: 10.3221/IGF-ESIS.30.67.

[29] C. Santus, D. Taylor, and M. Benedetti, "Determination of the fatigue critical distance according to the Line and the Point Methods with rounded V-notched specimen," *Int. J. Fatigue*, vol. 106, pp. 208–218, Jan. 2018, doi: 10.1016/j.ijfatigue.2017.10.002.

[30] M. Benedetti and C. Santus, "Statistical properties of threshold and notch derived estimations of the

critical distance according to the line method of the theory of critical distances," *Int. J. Fatigue*, vol. 137, p. 105656, Aug. 2020, doi: 10.1016/j.ijfatigue.2020.105656.

[31] M. Benedetti, V. Fontanari, M. Bandini, F. Zanini, and S. Carmignato, "Low- and high-cycle fatigue resistance of Ti-6Al-4V ELI additively manufactured via selective laser melting: Mean stress and defect sensitivity," *Int. J. Fatigue*, vol. 107, pp. 96–109, Feb. 2018, doi: 10.1016/j.ijfatigue.2017.10.021.

[32] J.-C. He, S.-P. Zhu, D. Liao, X.-P. Niu, J.-W. Gao, and H.-Z. Huang, "Combined TCD and HSV approach for probabilistic assessment of notch fatigue considering size effect," *Eng. Fail. Anal.*, vol. 120, p. 105093, Feb. 2021, doi: 10.1016/j.engfailanal.2020.105093.

[33] Nadot, Mendez, Ranganathan, and Beranger, "Fatigue life assessment of nodular cast iron containing casting defects," *Fatigue Fract. Eng. Mater. Struct.*, vol. 22, no. 4, pp. 289–300, Apr. 1999, doi: 10.1046/j.1460-2695.1999.00162.x.

[34] Y. Nadot, "Influence of casting defects on the fatigue limit of nodular cast iron," *Int. J. Fatigue*, vol. 26, no. 3, pp. 311–319, Mar. 2004, doi: 10.1016/S0142-1123(03)00141-5.

[35] E. Foglio, D. Lusuardi, A. Pola, G. M. La Vecchia, and M. Gelfi, "Fatigue design of heavy section ductile irons: Influence of chunky graphite," *Mater. Des.*, vol. 111, pp. 353–361, Dec. 2016, doi: 10.1016/j.matdes.2016.09.002.

[36] T. Borsato, P. Ferro, A. Fabrizi, F. Berto, and C. Carollo, "Long solidification time effect on solution strengthened ferritic ductile iron fatigue properties," *Int. J. Fatigue*, vol. 145, p. 106137, Apr. 2021, doi: 10.1016/j.ijfatigue.2020.106137.

[37] S. Carmignato, "Accuracy of industrial computed tomography measurements: Experimental results from an international comparison," *CIRP Ann.*, vol. 61, no. 1, pp. 491–494, 2012, doi: 10.1016/j.cirp.2012.03.021.

[38] F. Zanini and S. Carmignato, "Two-spheres method for evaluating the metrological structural resolution in dimensional computed tomography," *Meas. Sci. Technol.*, vol. 28, no. 11, p. 114002, Nov. 2017, doi: 10.1088/1361-6501/aa85b7.

[39] J. J. Lifton and S. Carmignato, "Simulating the influence of scatter and beam hardening in dimensional computed tomography," *Meas. Sci. Technol.*, vol. 28, no. 10, p. 104001, Oct. 2017, doi: 10.1088/1361-6501/aa80b2.

[40] L. A. Feldkamp, L. C. Davis, and J. W. Kress, "Practical cone-beam algorithm," *J. Opt. Soc. Am. A*, vol. 1, no. 6, p. 612, Jun. 1984, doi: 10.1364/JOSAA.1.000612.

[41] M. Klesnil and P. Lukáš, "Influence of strength and stress history on growth and stabilisation of fatigue cracks," *Eng. Fract. Mech.*, vol. 4, no. 1, pp. 77–92, Mar. 1972, doi: 10.1016/0013-7944(72)90078-1.

[42] *European Standard EN 1563:2011. Founding—spheroidal graphite cast iron.* Brussel, Belgium: CEN, 2011.

[43] S. Beretta and Y. Murakami, "Statistical analysis of defects for fatigue strength prediction and quality

control of materials," *Fatigue Fract. Eng. Mater. Struct.*, vol. 21, no. 9, pp. 1049–1065, Sep. 1998, doi: 10.1046/j.1460-2695.1998.00104.x.

[44] M. Benedetti and C. Santus, "Mean stress and plasticity effect prediction on notch fatigue and crack growth threshold, combining the theory of critical distances and multiaxial fatigue criteria," *Fatigue Fract. Eng. Mater. Struct.*, vol. 42, no. 6, pp. 1228–1246, Jun. 2019, doi: 10.1111/ffe.12910.

Figure

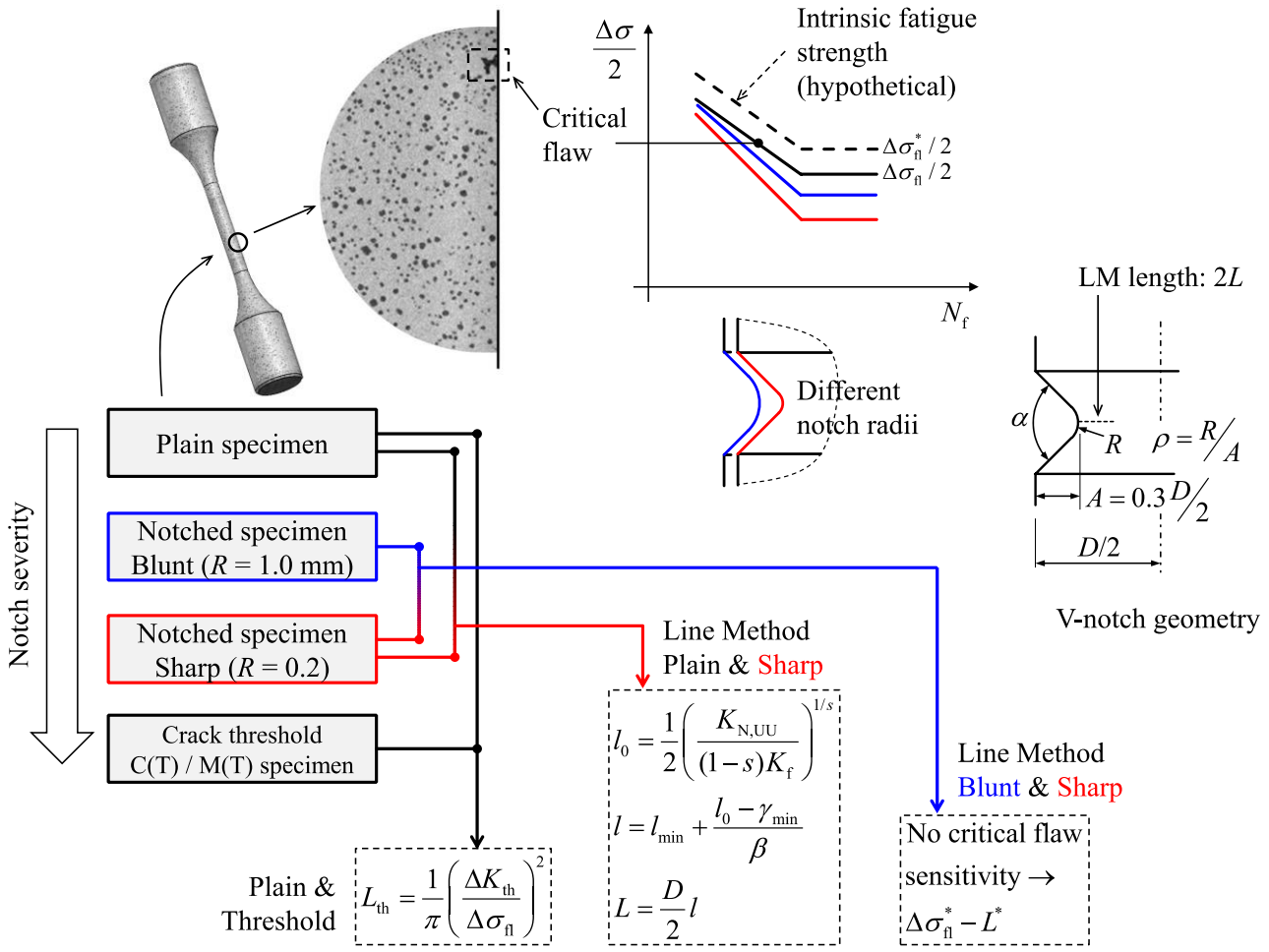

Figure 1: strategies for inverse search of the critical distance pursued in the present paper. (i) in "Plain&Treshold" L_{th} is deduced from plain fatigue strength and crack growth threshold, (ii) in "Plain&Sharp" L is obtained from the fatigue strength measured on a plain and an optimized notched geometry, (iii) in "Blunt&Sharp" L^* is determined from two optimized notched geometries producing a different stress concentration factor.

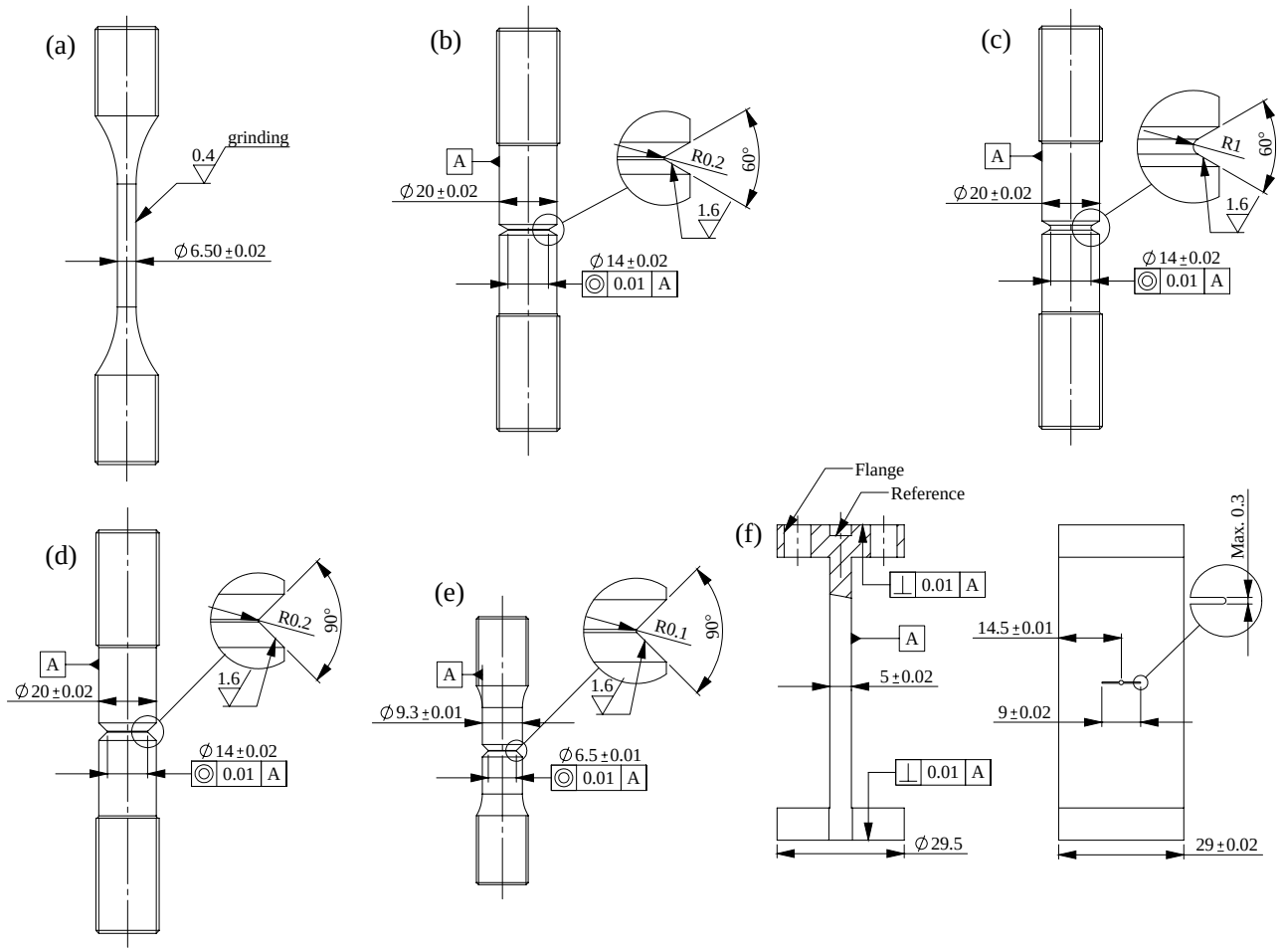

Figure 2. Geometry of the specimens used for the fatigue characterization. (a) plain, (b)-(e) notched specimens. (f) M(T) specimen used for the fatigue crack growth experiment. Dimension in mm. Fatigue data obtained from specimen geometries (b) and (c) were used to determine the critical distance L^* according to Blunt&Sharp approach specifically devised in the present work.

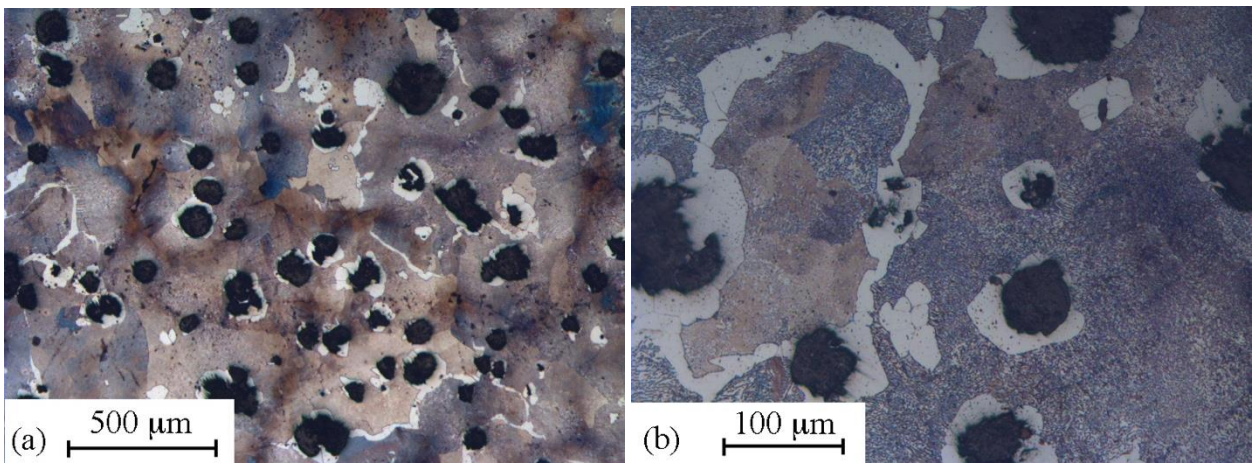

Figure 3. Microstructure of the EN-GJS-600-3 coupons cast investigated in this work shown at two magnification scales.

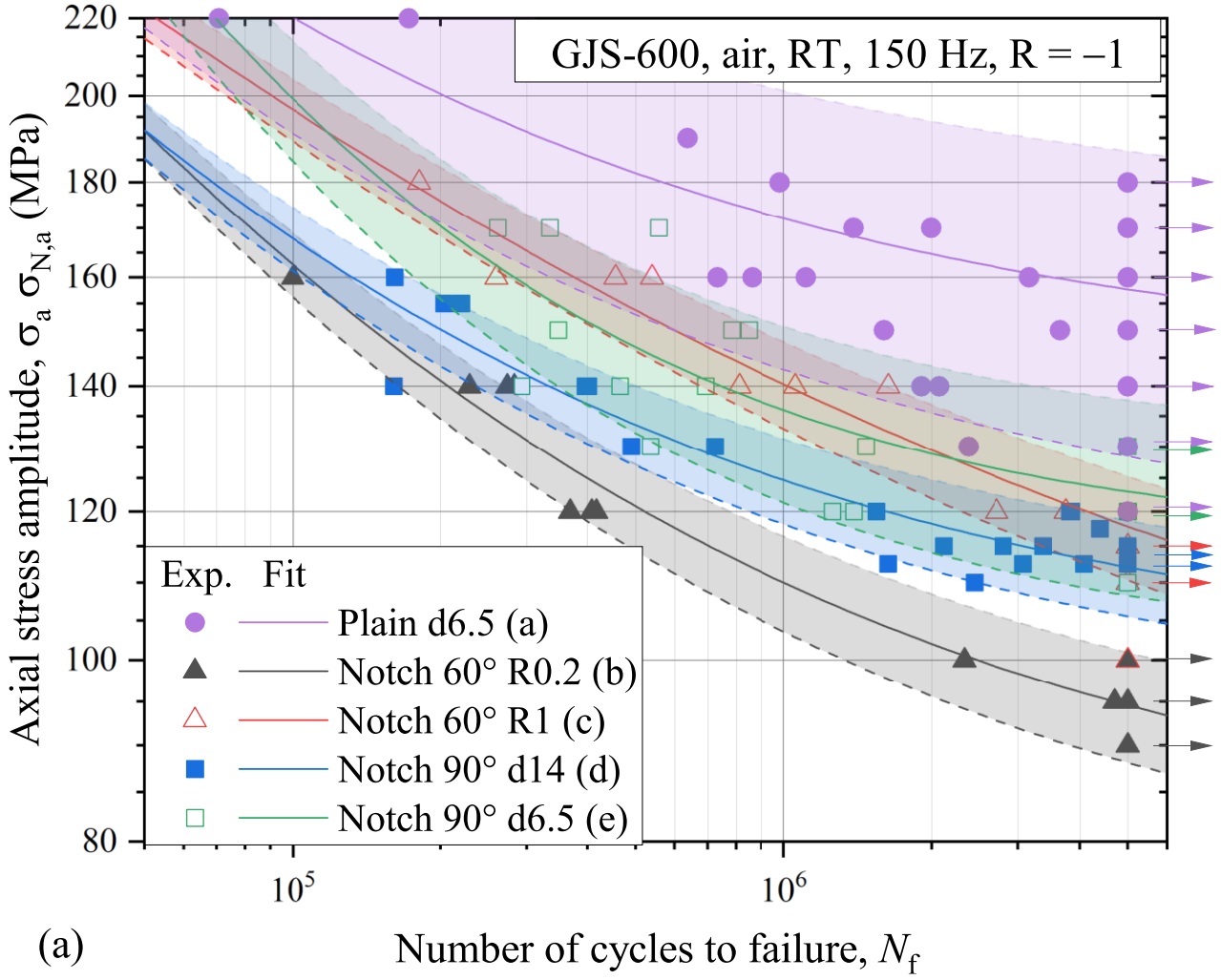
GJS-600, air, RT, 150 Hz, R = –1
Axial stress amplitude, σ_a $\sigma_{N,a}$ (MPa)
220
200
180
160
140
120
100
80
10^5
10^6
Exp. Fit
Plain d6.5 (a)
Notch 60° R0.2 (b)
Notch 60° R1 (c)
Notch 90° d14 (d)
Notch 90° d6.5 (e)
Number of cycles to failure, N_f

(a)

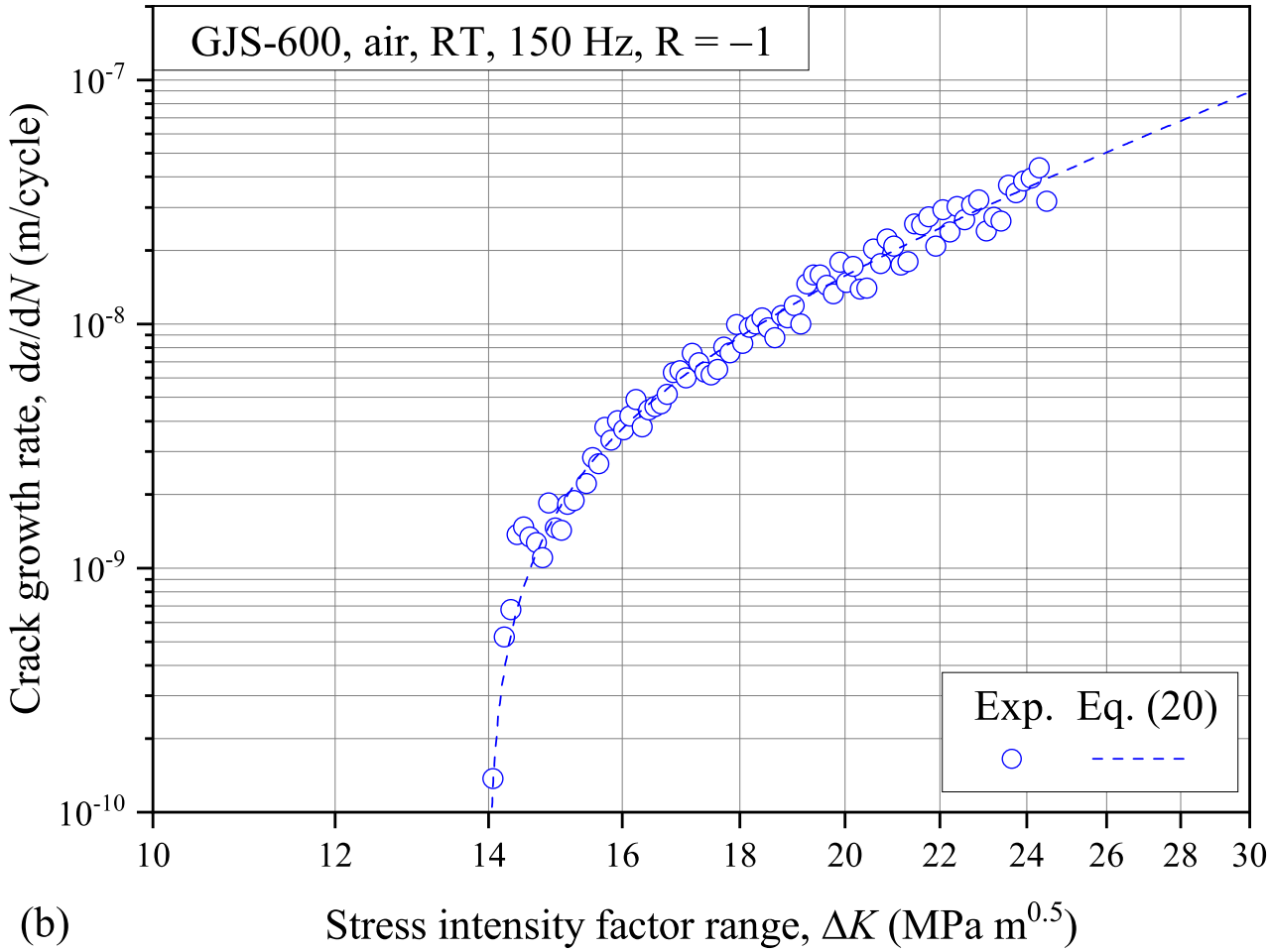

Figure 4. (a) Axial fatigue SN curves. Solid lines represent 50% failure probability, while dashed lines refer to 10% and 90% failure probability. Arrows indicated runout tests. (b) Fatigue crack propagation curve and Klesnil and Lukáš fit curve (Eq. (20)).

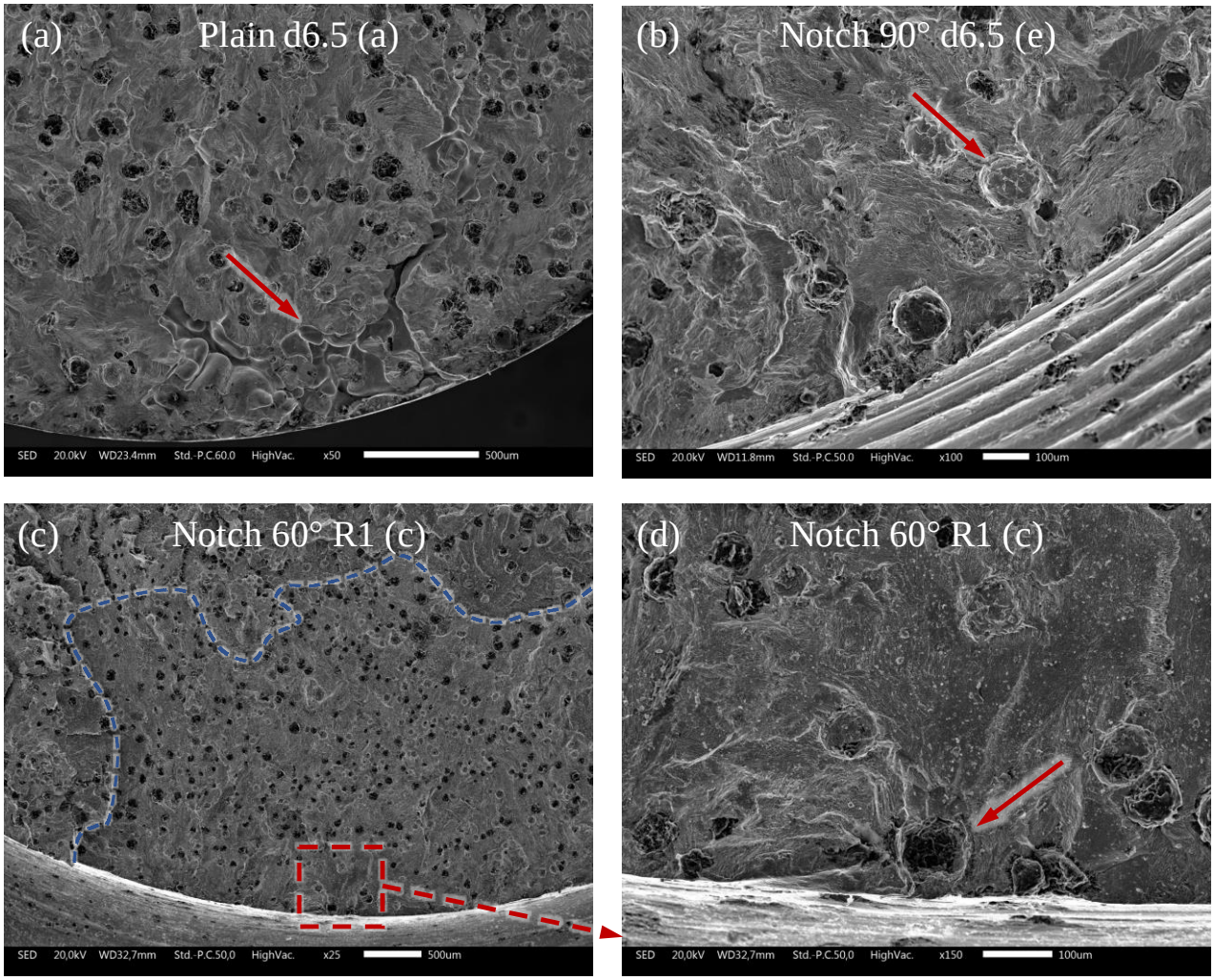

Figure 5: SEM micrographs of the fracture surfaces around the fatigue crack initiation site. (a) microshrinkage pore (red arrow) found in plain sample (a) (σ_a = 140 MPa, $N_f = 1.9\times10^6$). (b) Graphite nodule (red arrow) that likely triggered the fatigue crack initiation in notched specimen (d) (σ_a = 130 MPa, $N_f = 5.4\times10^5$). (c) and (d) fracture surface of a runout blunt notched specimen (c) ((σ_a = 110 MPa, $N_f = 5\times10^6$). (c) Dashed line indicates the front of the non-propagating crack revealed after fatigue resting at load ratio R = 0.1. (d) magnification of the detail enclosed in (c) by the red dashed rectangle. The red arrows indicate the graphite nodule causing the crack initiation in the runout test.

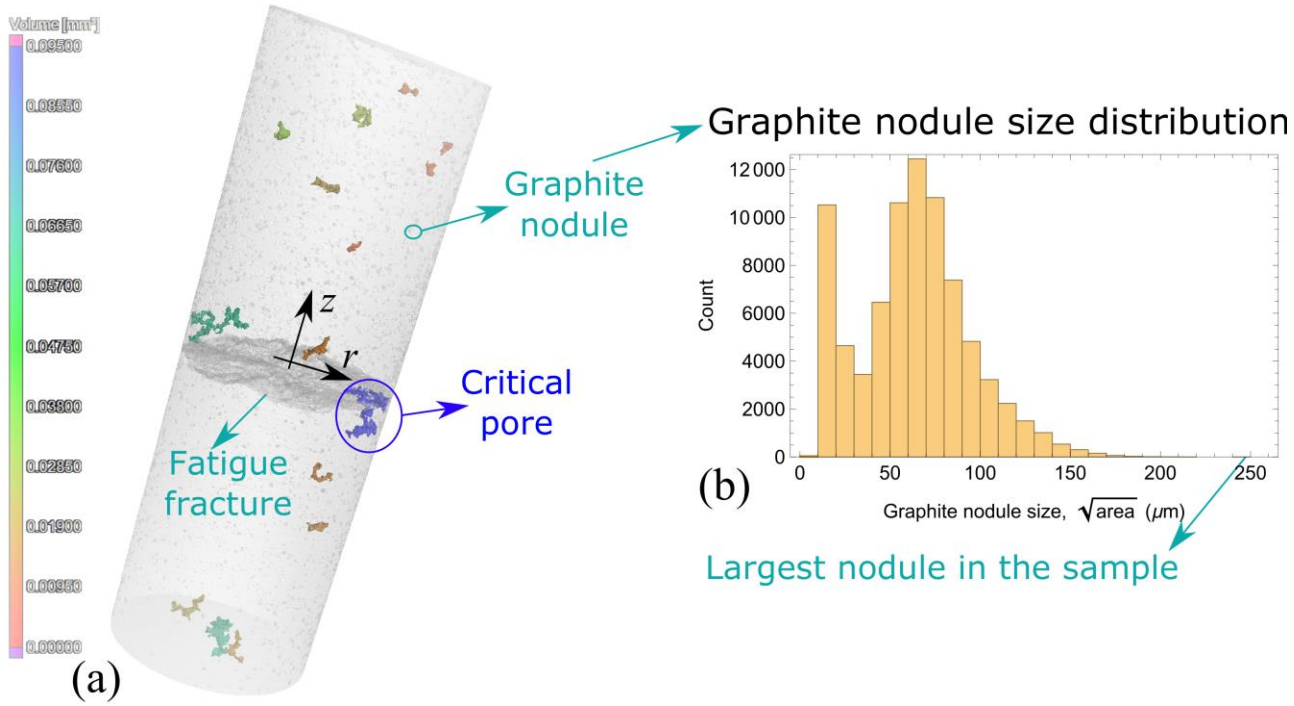

Figure 6. (a) CT scan of a plain sample (a). Shrinkage pores are indicated in color scale. The circled pore triggered the fatigue fracture shown in the CT scan. Grey features are graphite nodules. (b) Histogram showing the distribution of the Murakami $\sqrt{area}$ parameter of the graphite nodules detected in (a).

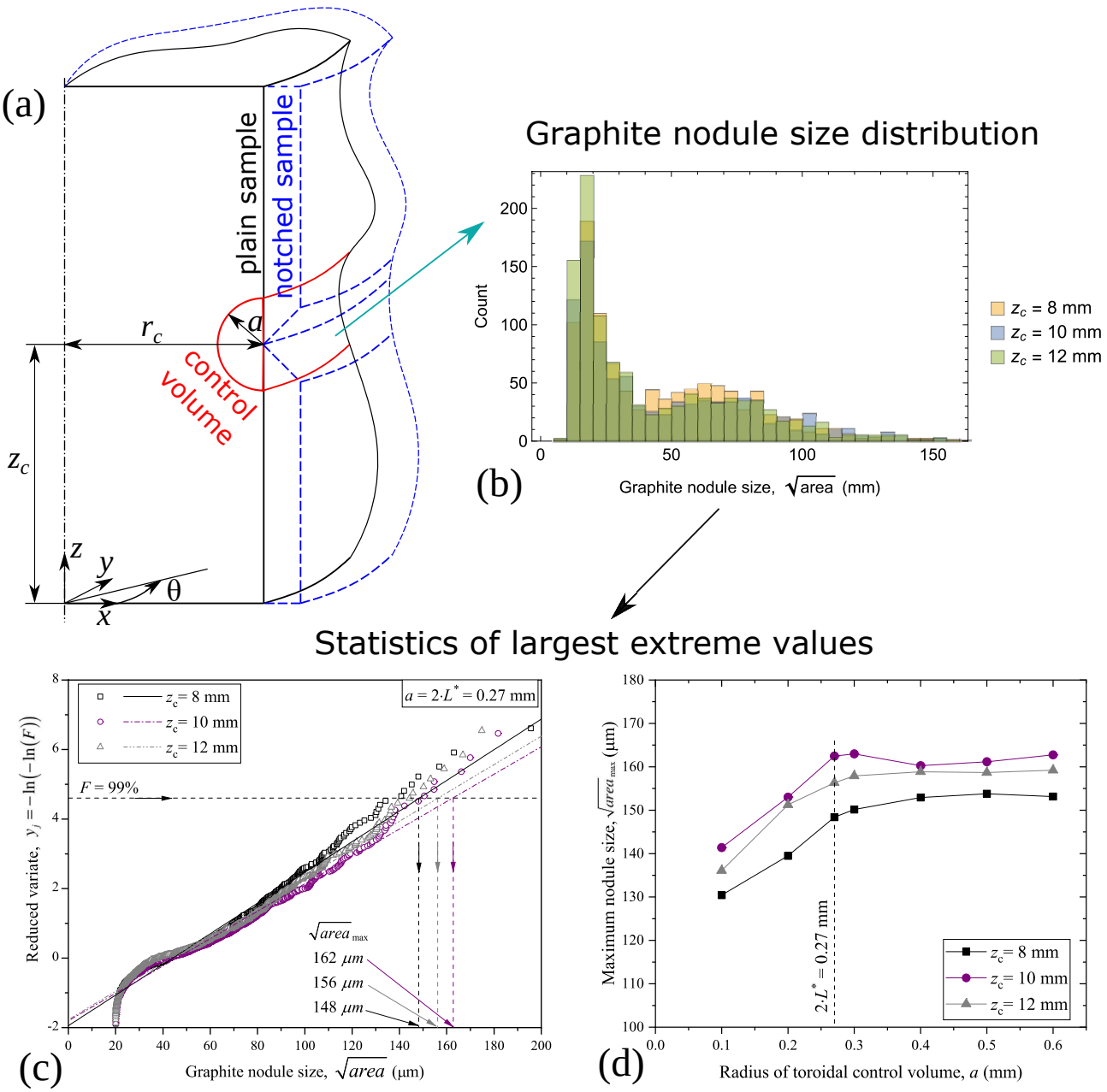

Figure 7. (a) geometry and location of the toroidal control volume considered for the estimation of the expected maximum size of the graphite nodule in the vicinity of the notch tip. For this purpose, the entire scanned volume of a plain sample (black line) is considered. The control volume is centered at the tip of the notched specimen (blue dashed line) having the same net section diameter as the plain specimen. (b) Histograms showing the distribution of the Murakami $\sqrt{area}$ parameter of the graphite nodules detected in control volumes located at different axial coordinate z from the fracture surface shown in Fig. 6. (c) Cumulative probability distributions of nodule dimension $\sqrt{area}$ detected in toroidal control volumes of different location *z*. (d) Maximum expected nodule size $\sqrt{area}_{max}$ as a function of the radius of the toroidal control volume.

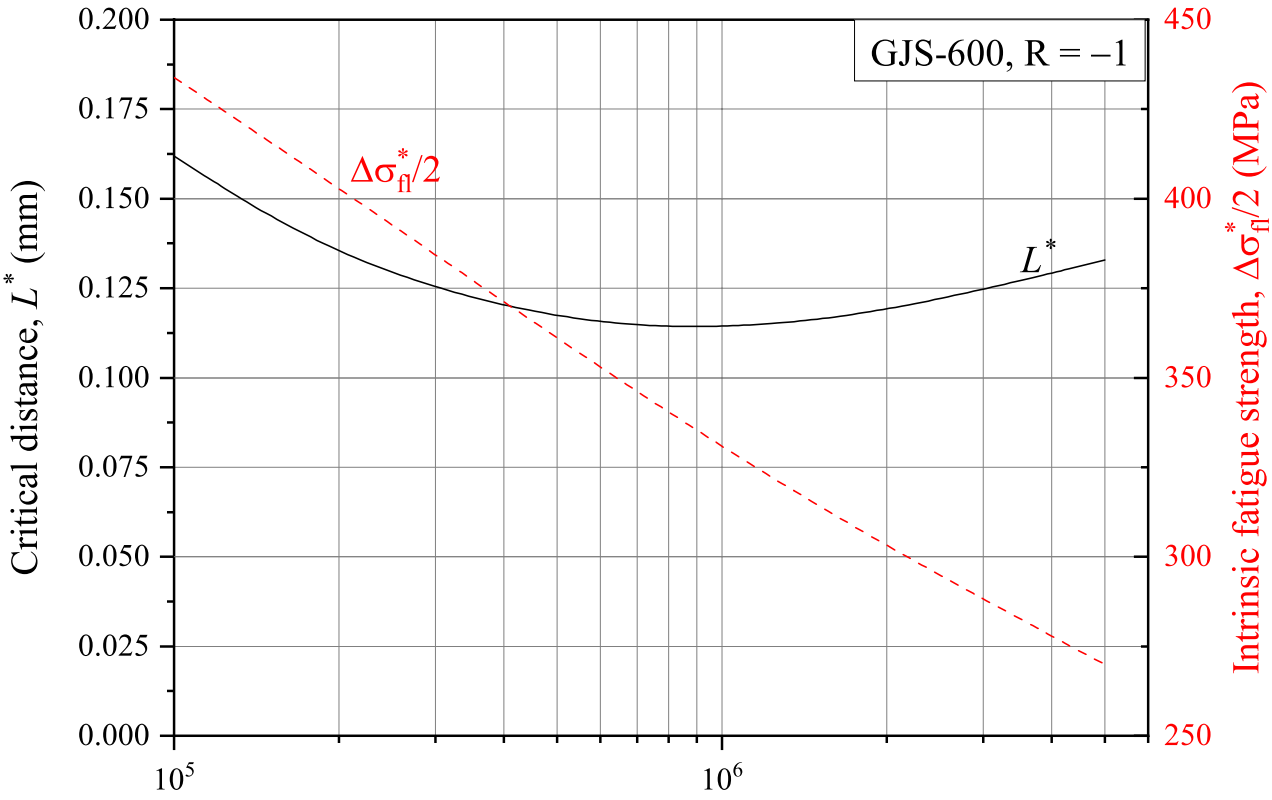
GJS-600, R = –1
$\Delta\sigma_{fl}^{*}/2$
L^{*}
Critical distance, L^{*} (mm)
Intrinsic fatigue strength, $\Delta\sigma_{fl}^{*}/2$ (MPa)
Number of cycles to failure, N_f
0.200
0.175
0.150
0.125
0.100
0.075
0.050
0.025
0.000
450
400
350
300
250
10^5
10^6

(a)

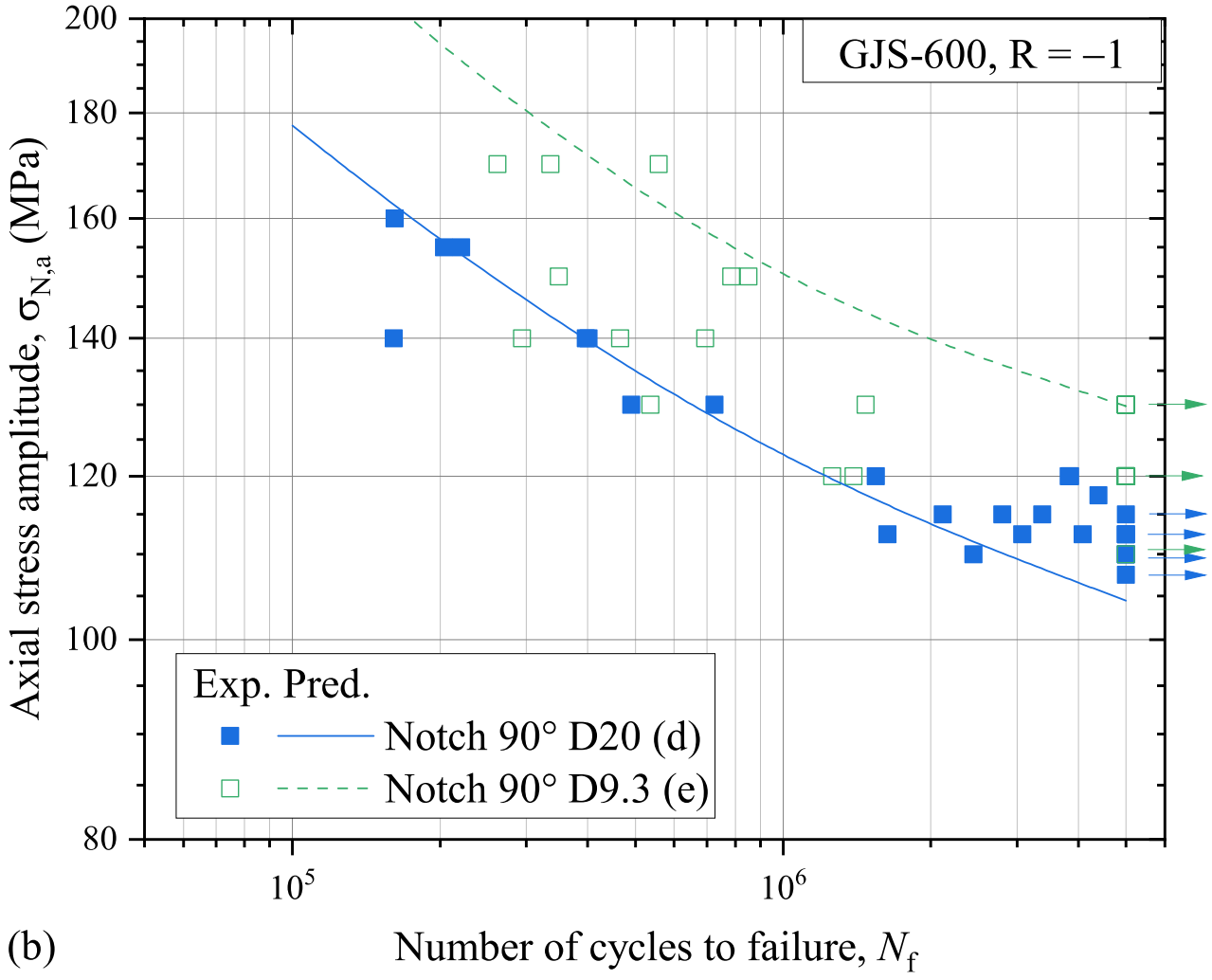

Figure 8: (a) critical distance L^* and intrinsic plain fatigue strength $\Delta\sigma_{fl}^*/2$ assessed according to the "Blunt&Sharp" method as a function of the number of cycles to failure. (b) Prediction of the fatigue curves of independent notched variants (d) and (e) not used for the calibration of the critical distance approach.

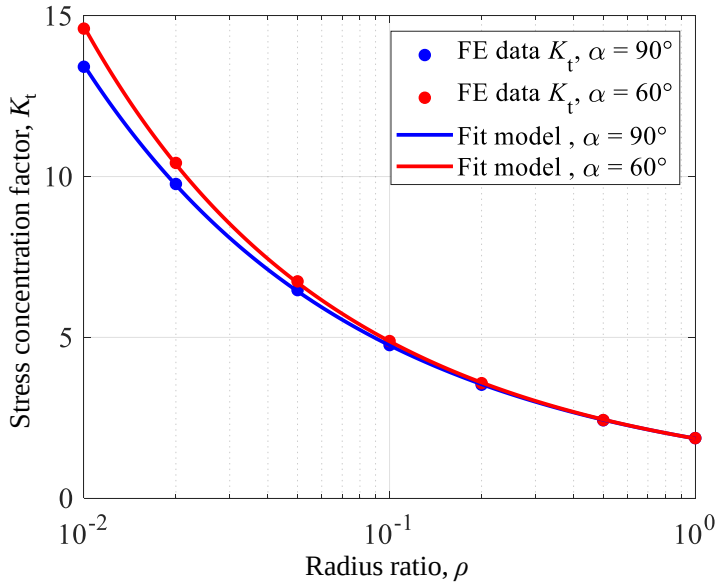

Fig. A.1. Stress concentration factor for the optimized specimens with notch angles $\alpha = 90°$ and $60°$ as functions of the notch radius ratio ρ.

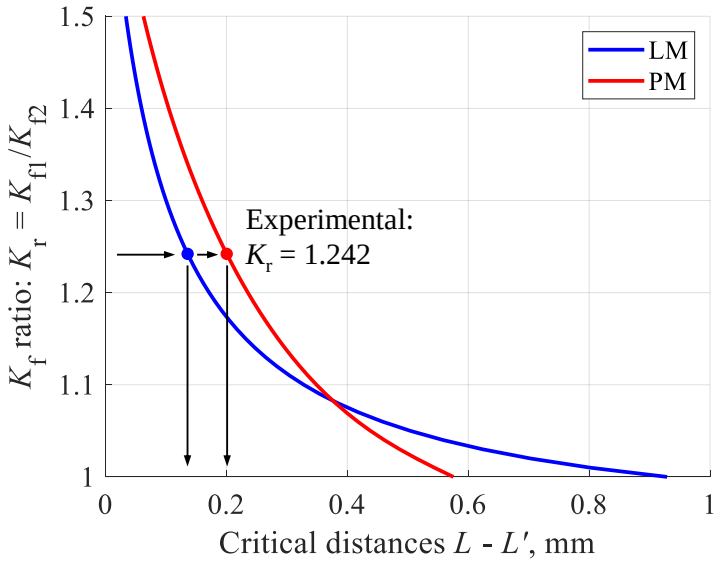

Fig. A.2. Example of LM and PM critical distance determinations, as functions of the fatigue stress concentration factor ratio K_r.

Tables

Table 1. Measured chemical composition (wt.-%) of the investigated EN-GJS-600-3 cast iron, balance Fe.

C	**Si**	**Mn**	**P**	**S**	**Cu**	**Ni**	**Mg**
3.550	2.390	0.280	0.038	0.009	0.520	0.020	0.046

Table 2. Notch root radius measured in the notched variants and corresponding stress concentration factor.

Specimen geometry	Notch root radius (mm)	Theoretical stress concentration factor K_t
Notch 60° R0.2 (b)	0.30±0.01	4.95
Notch 60° R1 (c)	1.00±0.01	2.87
Notch 90° d14 (d)	0.51±0.03	3.87
Notch 90° d6.5 (e)	0.17±0.01	4.48

Table 3. Results of the 2D optical analyses of the graphite nodules. Standard error corresponds to 1σ uncertainty band.

Number of nodules	Total graphite content (%)	Fraction of spheroidal graphite (%)	Diameter of graphite nodules d_G (μm)	Shape factor f_0	Roundness ρ_G	Mean nearest-neighbour distance λ_{nn} (μm)
1965	13±2	98±1	62±40	0.90±0.20	0.61±0.15	104±43

Table 4. Monotonic tensile properties and Brinell hardness (based on four replicated tests). Standard error corresponds to 1σ uncertainty band.

Condition	S_Y (MPa)	S_U (MPa)	T.E. (%)	HB
present material	363±8	458±15	2.1±0.5	198±4
EN-GJS-600-3 [42] 60 < t ≤ 200 mm	320 min	500 min	1 min	190 ÷270
S_Y: 0.2% yield stress; S_U: ultimate tensile strength; T.E.: total elongation; HB: Brinell hardness				

Table 5. Best-fit coefficients of Eq. (16) used to interpolate the SN curves. *S* indicates the standard deviation. The high-cycle fatigue strength was assessed at 5×10^6 cycles.

Specimen geometry	k_1 (MPa)	k_2 (MPa)	k_3	*S* (MPa)	$\Delta\sigma_{fl}/2,\ \Delta\sigma_{N,fl}/2$ at 5×10^6 cycles (MPa)
Plain d6.5 (a)	143	10205	0.424	23	158 (158±19*)
Notch 60° R0.2 (b)	79.2	12062	0.432	5.0	94.6
Notch 60° R1 (c)	78.2	2980.9	0.280	5.8	118
Notch 90° d14 (d)	99.6	10078	0.434	5.1	112 (113±2*)

Notch 90° d6.5 (e)	115	89358	0.605	11	123 (124±15*)
* mean and standard deviation of the fatigue endurance estimated on the base of a staircase approach					

Table 6. Best-fit parameters of the crack propagation law expressed by Eq. (20)

Specimen geometry	ΔK_{th} (MPa·m$^{0.5}$)	C	m (*)
M(T) (f)	14.0	3.75×10^{-13}	3.66
Units in Eq. (20) are m/cycle and MPa·m$^{0.5}$			

Table 7: Results of the critical distance inversion methods illustrated in Fig. 1.

Plain&Threshold Specimen geometry: (a) & (f)		Plain&Sharp (a) & (b)		Blunt&Sharp (c) & (b)	
$\Delta\sigma_{fl}/2$ (MPa)	L_{th} (mm)	$\Delta\sigma_{fl}/2$ (MPa)	L (mm)	$\Delta\sigma^{*}_{fl}/2$ (MPa)	L^{*} (mm)
158	0.625	158	0.530	269	0.136

Table 8: Prediction of the notch fatigue strength and crack growth threshold of independent geometries not used in the calibration of the critical distance method.

Specimen geometry	Exp. (MPa/ MPam$^{0.5}$)	Plain&Threshold		Plain&Sharp		Blunt&Sharp	
		Pred.	Err. (%)	Pred.	Err. (%)	Pred.	Err. (%)
Notch 60° R0.2 (b)	94.6	102	7.5	-	-	-	-
Notch 60° R1 (c)	118	105	-11	99.3	-16	-	-
Notch 90° d14 (d)	112	104	-7.2	97.5	-13	105	-6.4
Notch 90° d6.5 (e)	123	143	16	133.3	8.4	130	6.1
M(T) (f)	14.0	-	-	12.9	-7.9	11.1	-20

Table 9. Results of the 3D analyses done via CT scans of pores and graphite nodules. Standard error corresponds to 1σ uncertainty band.

Type of feature	Number of detected features	Diameter d^{*} (μm)	Sphericity ϕ
pore	14	333±84	0.25±0.07

graphite nodule	68537	65±31	0.54±0.07

Table 10. Prediction of the fatigue strength of the control volume based on the maximum expected nodule size according to the models expressed in Eq. (21).

F_{loc}	HV*	S_U (MPa)	S_Y (MPa)	$\sqrt{area}_{max}$ (μm)	σ_W (MPa)		
					Murakami [8]	Deguchi et al. [10]	Borsato et al. [11]
1.56	198	458	363	155	214	219	269
* estimated through conversion from Brinell hardness							

Table A.1. Fit coefficients of the K_t model for the two considered notch angles.

Notch angle α	t_1	t_2	t_3
90°	0.02206	-0.3862	0.2687
60°	0.02912	-0.3907	0.2685